



Draft Manuscript for Review

**Effect of water activity on reaction kinetics and
intergranular transport:
Insights from the $\text{Ca}(\text{OH})_2 + \text{MgCO}_3 \rightarrow \text{CaCO}_3 + \text{Mg}(\text{OH})_2$
reaction at 1.8 GPa**

Journal:	<i>Journal of Petrology</i>
Manuscript ID	JPET-Jan-15-0005.R3
Manuscript Type:	Original Manuscript
Date Submitted by the Author:	29-Jun-2016
Complete List of Authors:	Gasc, Julien; Ecole Normale Supérieure, Laboratoire de Géologie; CNRS, Geosciences Montpellier Brunet, Fabrice; Univ. Grenoble Alpes, CNRS, ISTERRE Brantut, Nicolas; University College London, Rock and Ice Physics Laboratory, Department of Earth Sciences Corvisier, Jérôme; Mines ParisTech, Centre de Géosciences Findling, Nathaniel; Université Grenoble Alpes, ISTERRE Verlaguet, Anne; Université Pierre et Marie Curie, ISTEP Lathe, Christian; GeoForschungZentrum, Hasylab - Desy
Keyword:	water, experimental petrology, metamorphic petrology, carbonate

SCHOLARONE™
Manuscripts

1
2
3
4 1 **Effect of water activity on reaction kinetics and intergranular transport:**

5
6 2 **Insights from the $\text{Ca(OH)}_2 + \text{MgCO}_3 \rightarrow \text{CaCO}_3 + \text{Mg(OH)}_2$ reaction at 1.8 GPa**

7
8
9 3
10
11
12 4
13
14
15 5 **Authors**

16
17 6 Julien GASC¹

18
19
20 7 Laboratoire de Géologie, École normale supérieure, CNRS-UMR8538, Paris, France

21
22 8
23
24 9 Fabrice BRUNET[✉]

25
26
27 10 **Université Grenoble Alpes, CNRS, ISTERRE,** Grenoble, France

28
29
30
31
32 12 Nicolas BRANTUT

33
34 13 Earth Sciences Department, University College London, UK

35
36
37
38
39 15 Jérôme CORVISIER

40
41 16 Centre de Géosciences, Mines ParisTech, Fontainebleau, France

42
43
44
45
46 18 Nathaniel FINDLING

47
48 19 **Université Grenoble Alpes, ISTERRE,** Grenoble, France

49
50
51
52
53 21 Anne VERLAGUET

54
55
56 22 ISTeP, – Université Pierre et Marie Curie, 4 place Jussieu, Paris, France

1
2
3 23
4
5
6 24 Christian LATHE
7
8 25 GFZ, Telegraphenberg, D-14473 Potsdam, Germany
9
10
11 26
12
13 27 ¹Current Address: Géosciences Montpellier, Université de Montpellier-CNRS, Montpellier, France
14
15 28 ✉ TEL : +33 476 514 106, Fax: +33 476 635 252 e-mail : fabrice.brunet@univ-grenoble-alpes.fr
16
17
18 29
19
20
21
22
23
24
25
26
27
28
29
30
31
32
33
34
35
36
37
38
39
40
41
42
43
44
45
46
47
48
49
50
51
52
53
54
55
56
57
58
59
60

For Peer Review

30 **ABSTRACT**

31 The kinetics of the irreversible reaction $\text{Ca(OH)}_2 + \text{MgCO}_3 \rightarrow \text{CaCO}_3 + \text{Mg(OH)}_2$ were investigated
32 at high pressures and temperatures relevant to metamorphic petrology, using both in-situ synchrotron
33 X-ray diffraction and post-mortem analysis of reaction rims growth on recovered samples. Reaction
34 kinetics are found to strongly depend on water content; comparable bulk-reaction kinetics are obtained
35 under water *saturated* (excess water, ca. 10 wt.%) and under *intermediate* (0.1-1 wt.% water) conditions
36 when temperature is increased by ca. 300 K. Whereas, similar reaction kinetics were observed at ~673 K
37 and 823 K between *intermediate* and *dry* experiments, respectively, where *dry* refers to a set of
38 experiments with water activity below one (no free water), as buffered by the CaO-Ca(OH)₂ assemblage.
39 Given the activation energies at play, this gap –corresponding to the loss of no more than 1 wt.% of
40 water by the assemblage– leads to a difference of several orders of magnitude in reaction kinetics at a
41 given temperature.

42 Further analysis, at the microscopic scale, of the *intermediate* and *dry* conditions samples, shows
43 that intergranular transport of calcium controls the reaction progress. Grain boundary diffusivities could
44 be retrieved from the classic treatment of reaction rim growth rate. In turn, once modeled, this rate was
45 used to fit the bulk kinetic data derived from XRPD, offering an alternative mean to derive calcium
46 diffusivity data. Based on a comparison with effective grain boundary data for Ca and Mg from the
47 literature, it is inferred that both *dry* and *intermediate* datasets are consistent with a water saturated
48 intergranular medium with different levels of connectivity. The very high diffusivity of Ca in the CaCO₃ +
49 Mg(OH)₂ rims, in comparison that of Mg in enstatite rims [Gardés et al., *Contributions to Mineralogy and*
50 *Petrology* 164; 2012], emphasizes the prominent role of the interactions between diffusing species and
51 mineral surfaces on diffusion kinetics. Furthermore, we show that the addition of water is likely to
52 change the relative diffusivity of Mg and Ca in carbonate aggregates. On a qualitative point of view, we
53 confirm, in a carbonate-bearing system, that small water content variations within the 0 - 1 wt. % range,
54 have tremendous effects on both intergranular transport mechanisms and kinetics. We also propose
55 that the water-content dependent diffusivity of major species (Mg, Ca) in low-porosity metamorphic
56 rocks is strongly dependent of the interaction between diffusing species and mineral surfaces. This
57 parameter which will vary from one rock-type to the other, needs also to be considered when extrapolating
58 (P,T,t, xH₂O) laboratory diffusion data to metamorphic processes.

59 **Keywords:** metamorphic reaction, kinetics, intergranular transport, water, calcium diffusion

60 INTRODUCTION

61
62 The kinetics of metamorphic reactions is strongly dependent on temperature, grain size and
63 water availability. The latter parameter is probably the most difficult to quantify, especially over the
64 course of a whole metamorphic cycle. The ubiquity of fluid during metamorphism has long been a
65 subject of controversy (Rubie, 1986, Thompson, 1983) and it is widely accepted now that variations of
66 water availability and content, in metamorphic rocks, is likely to account for the discrepancy between
67 natural reaction kinetics and those extrapolated from experimental data (Baxter, 2003). On the field, the
68 prominent role of water availability is supported by occurrences of partially eclogitized high-grade rocks
69 in which eclogitization took place in shear zones, where fluid infiltrated (Austrheim, 1987, John &
70 Schenk, 2003, Molina *et al.*, 2002). At a larger scale, by combining petrological and geophysical
71 constraints, Hetenyi *et al.* (2007) have suggested that the eclogitization of the Indian lower crust
72 beneath Tibet is delayed due to equilibrium overstepping until it is catalyzed by the release of water
73 from hydrous minerals.

74 Beyond the notion of water availability, which describes the intermittent presence of water in
75 the course of the metamorphic reaction process, the question of the effect of water content on the
76 reaction kinetics also appears to be relevant. In fact, most of the dataset of mineral reaction kinetics
77 available in the literature (phase relationship, dissolution, etc.) is based on experiments performed
78 under hydrothermal conditions with large water/rock ratios. Consequently, when extrapolated to
79 nature, assuming permanent water availability, this type of experimental data predicts that
80 metamorphic reaction rates are fast and that the preservation of metastable mineral assemblages
81 (reaction equilibrium overstep) is short with respect to metamorphic timescales (Wood & Walther,
82 1983). Although possibly valid for metapelites transforming along their prograde path, this conclusion
83 does not necessarily hold for high-grade rocks (e.g., upper amphibolite or granulite facies rocks) reacting
84 back with water. Under these latter circumstances, Yardley and Valley (1997) showed, on
85 thermochemical grounds, that excess water conditions (i.e.; water saturation) are not met and that
86 water activity must be below unity (taking as reference state pure water at T and P). In parallel, it has
87 been shown recently that even minute amounts of water can have a drastic effect on the kinetics of
88 mineral reactions through the enhancement of mass transport (Milke *et al.*, 2013; Gardés *et al.*, 2012,
89 Joachim *et al.*, 2012, Carlson, 2010, Milke *et al.*, 2009). In fact, a full range of intergranular diffusion
90 regimes has been identified as a function of water content (Farver & Yund, 1995, Rubie, 1986) between
91 the “dry” and the “water saturated” end member cases. These regimes are characterized by a range of

1
2
3 92 grain boundary diffusivities that can span over seven orders of magnitude in the case of aluminum
4
5 93 (Carlson, 2010). Even though Gardés et al. (2012) proposed a microscopic description for each of these
6
7 94 intergranular diffusion regimes, the physical state of water below the 1 wt.% level remains largely
8
9 95 unknown under metamorphic pressures and temperatures. Furthermore, studies addressing the effect
10
11 96 of low water contents on intergranular transport and its implications for mineral reaction rates are
12
13 97 scarce although of high geological relevance. The in-situ characterization at high pressure and
14
15 98 temperature (PT) of the physico-chemical properties of intergranular water present in very low
16
17 99 concentrations is obviously a difficult task. Gasc et al. (2011), for example, used in-situ impedance
18
19 100 spectroscopy at 2 GPa to characterize the electrical properties (diffusivity of electrical charge carriers) of
20
21 101 the intergranular region of a brucite polycrystal as a function of temperature for various water contents.
22
23 102 Using the $\text{CaO} - \text{Ca}(\text{OH})_2$ and $\text{MgO} - \text{Mg}(\text{OH})_2$ equilibria to buffer the water activity in the samples, the
24
25 103 authors were able to show that grain-boundary conductivity can vary by seven orders of magnitude
26
27 104 upon water content. In the present study, we propose to use a similar water buffering strategy to
28
29 105 address the effect of low water content variation on intergranular transport in the course the $\text{Ca}(\text{OH})_2 +$
30
31 106 $\text{MgCO}_3 \rightarrow \text{CaCO}_3 + \text{Mg}(\text{OH})_2$ reaction at 1.8 GPa. A special attention will be paid to bridge bulk and
32
33 107 microscopic approaches so that reaction kinetics derived from time-resolved x-ray powder diffraction
34
35 108 (XRPD) will be compared to growth rate of $\text{CaCO}_3 + \text{Mg}(\text{OH})_2$ rims around coarse magnetite (MgCO_3)
36
37 109 grains dispersed in a fine portlandite, $\text{Ca}(\text{OH})_2$, matrix. All terms and symbols used throughout the text
38
39 110 are defined in Table 1.
40
41
42
43
44
45
46
47
48
49
50
51
52
53
54
55
56
57
58
59
60

112 EXPERIMENTAL

113 Experimental strategy

114

115 Cubic multi-anvil (DIA) experiments were performed at 1.8 GPa in a range of temperatures (393 –
116 873 K), run durations and water contents on the non-reversible exchange reaction:



118

119 This reaction was chosen for its relatively fast kinetics, even under severely dry conditions, in order to
120 allow investigation of its kinetics *in situ* from time-resolved synchrotron diffraction. Additional
121 experiments were also performed in a piston-cylinder (PC) apparatus to investigate the kinetics of
122 reaction (1) under water-saturated conditions at the same pressure, in sealed gold containers.

123 The recovered MA samples (i.e., *dry* and *intermediate*) were characterized using Scanning
124 Electron Microscopy (SEM) with a Zeiss® Field-effect SEM (FE-SEM), which showed the presence of
125 reaction rims around coarse residual magnesite grains. The kinetics of chemical transport across the rim-
126 forming polycrystalline material, composed of brucite, Mg(OH)_2 , and aragonite, CaCO_3 , was
127 characterized from the determination of rim growth rates as well as from one-dimension diffusion
128 experiments performed with the same starting material in the PC apparatus. Grain boundary diffusion
129 coefficients, $\bar{D}^{GB}\delta$, were retrieved from both datasets using a segregation factor set to one, since major
130 element diffusion is involved.

131 Finally, the two approaches (i.e., bulk reaction kinetics and chemical transport at the reaction
132 rim scale) were bridged. Grain boundary diffusion coefficients were refined to fit the time-resolved
133 synchrotron diffraction data; the diffusion coefficients obtained in this fashion were then compared to
134 those retrieved from the growth rate of reaction rims and reaction fronts (FE-SEM data), in order to test
135 the consistency between microscopic and bulk datasets.

136

137 Starting materials

138

139 The starting material was a mixture of natural magnesite, MgCO_3 , and synthetic portlandite,
140 Ca(OH)_2 . Portlandite was synthesized hydrothermally (623 K, 150 MPa, 45 h) in a cold-seal vessel from
141 CaO, which was obtained by decarbonation of reagent grade calcite (Merck 2066 with <1% impurities) at

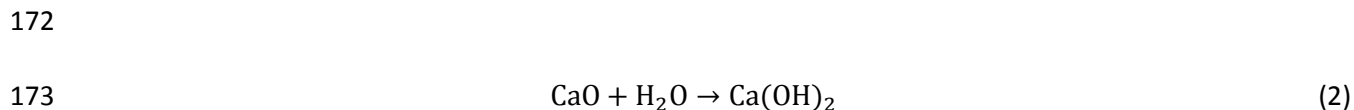
1
2
3 142 1273 K. Magnesite was extracted from a natural single crystal containing less than 1 wt.% CaO and FeO;
4
5 143 the absence of mineral impurity was checked by XRPD. Portlandite and magnesite were grinded
6
7 144 together in an agate mortar in equimolar proportions. SEM showed that the starting material was
8
9 145 composed of a fine-grained matrix (grain diameter less than 1 μm) with, sporadically, coarser magnesite
10
11 146 grains ($\sim 10 \mu\text{m}$). These larger grains are less reactive but, as described hereafter, are suitable for the
12
13 147 measurement of reaction rim growth rates.
14
15 148

17 149 **Reaction kinetics from in-situ synchrotron x-ray diffraction**

18
19 150

20 151 High PT experiments with in-situ energy dispersive XRPD were carried out using the MAX80 DIA
21
22 152 press (6 anvils cubic type multi-anvil) installed on beamline F2.1 at HasyLab. The starting powder was
23
24 153 pressed to a pellet (2 mm in diameter) and fitted into a boron nitride (BN) sleeve, which purpose was to
25
26 154 insulate chemically the sample from the graphite furnace but was not designed to retain water. The BN
27
28 155 sleeve was then fitted into a cylindrical graphite furnace and sandwiched between two dried NaCl
29
30 156 pellets used as pressure marker (Decker, 1971). Temperature was measured with a Type-N
31
32 157 thermocouple, the junction of which was located at a NaCl / sample interface. Boron-epoxy cubes with
33
34 158 8 mm edges were used as pressure medium in conjunction with 6 mm truncation WC anvils. Details of
35
36 159 the cell assembly and the MAX80 press can be found in Mueller (2003). Note that in order to minimize x-
37
38 160 ray absorption no sealed noble-metal container was used. Therefore, as described hereafter, water
39
40 161 saturated experiments were achieved separately in the PC using sealed gold container.

41 162 Two types of hydration levels were tested in the DIA experiments. The starting material was
42
43 163 either equilibrated with the air moisture before being loaded into the BN sleeve, or was dried at 383 K
44
45 164 and mixed together with about 5 wt.% CaO, a hygroscopic compound. In the former case, the amount of
46
47 165 adsorbed water onto the starting material can be estimated by weight loss through heating at 383 K and
48
49 166 was found to reach ca. 1 wt.%. These hydration conditions are referred to as *intermediate* hereafter.
50
51 167 Gasc et al. (2011) showed, using in-situ impedance spectroscopy on an $\text{Mg}(\text{OH})_2$ aggregate at 2 GPa, that
52
53 168 in a similar set-up where the sample is only partly sealed, such adsorbed water mostly remains in the
54
55 169 sample for several hours at temperature below ca. 980 K. In the case where CaO (lime) was added to
56
57 170 the oven-dried sample powder, residual free-water from the sample and its close environment was
58
59 171 removed below the set-point temperature by chemical drying following the reaction:
60



9
10
11 175 This method has been successfully used in Gasc et al. (2011), who showed progressive sample drying,
12 176 through CaO hydroxylation, as evidenced by a drop of the sample bulk electrical conductivity upon
13
14 177 heating at temperatures as low 673 K. Lime hydroxylation was similarly evidenced here by the
15
16 178 pronounced decrease of the CaO reflections intensity upon heating at $T > 500$ K, i.e., while the reaction
17
18 179 of interest (1) had not yet started (Figure 1). As long as CaO and Ca(OH)₂ are present in the sample, the
19
20 180 starting water activity is buffered to a value that depends on the free enthalpy of Reaction (2) and
21
22 181 therefore on temperature. The water activity was calculated using Wintwq 2.34 (Berman & Aranovich,
23
24 182 1996) in the 823–873 K temperature range corresponding to our experiments and was found to vary
25
26 183 from 0.1 to 0.15. These experiments, which involve chemical drying, will be called *dry* in the following.

27 184 A white x-ray beam provided by the DORIS III storage ring was used to collect energy dispersive
28
29 185 XRPD data. The spectra were collected continuously with acquisition times of 45 or 60 seconds (Figures
30
31 186 1 and 2) with a 2048 channels solid-state Ge detector. The Bragg reflection of highest intensity typically
32
33 187 varied from 2×10^3 to 5×10^3 detector counts.

34
35 188 Reaction progress, $\xi(t)$, was calculated for each spectrum collected at a time, t , from the
36
37 189 intensity, $I(t)$ of selected diffraction peaks, assuming that $\xi(t) = I(t)/I_{\max}$ for products and that $\xi(t) = 1 -$
38
39 190 $(I(t)/I_{\max})$ for reactants, where I_{\max} is the maximum intensity of the considered reflection (Lathe *et al.*,
40
41 191 2005, Zinn *et al.*, 1995). Therefore, for reactants, at $t = 0$, $\xi(t) = 0$ and $I(0) = I_{\max}$. We calculated reaction
42
43 192 progress either from the intensity of the (104) reflection of MgCO₃ or the (011) reflection of Ca(OH)₂
44
45 193 (Figure 2). Because of its larger grain size distribution, magnesite is less suitable for quantification
46
47 194 purposes using X-ray powder diffraction than portlandite, which was thus preferentially used to
48
49 195 calculate $\xi(t)$. Note that, with the use of white synchrotron light, the beam is collimated and the volume
50
51 196 sampled is relatively small, which, in some cases, may translate as an insufficient number of grains
52
53 197 sampled for proper quantitative analysis. This can cause the relative intensities of the diffraction peaks
54
55 198 to fluctuate and not represent the actual phase proportions. Therefore, whenever possible, reaction
56
57 199 progress was additionally retrieved from the (111) and (011) reflection intensities of CaCO₃ and
60
200 Mg(OH)₂, respectively. In all cases, intensities, I , were also subtracted a background that was estimated
201
for each t . The ratio between maximum peak intensity and background level was typically ~ 30 . In some

1
2
3 202 instances, after collection of kinetic data at a certain constant temperature, the experiment was
4
5 203 terminated by increasing further the temperature until $\xi(t) = 1$ was achieved, which allows retrieving I_{\max}
6
7 204 values for the reaction products and enables their use for calculating $\xi(t)$. In addition, the incident beam
8
9 205 intensity decayed with time due to the decrease of the storage ring current. In order to account for this
10
11 206 effect on peak intensities, and since the irradiated sample zone relative to the x-ray detector remains
12
13 207 unchanged during an experiment, the peak intensities were normalized to the BN (100) reflection
14
15 208 (Figure 2).

16 209 **Reaction kinetics with excess water**

17
18 210

19
20 211 The kinetics of the reaction was also investigated at lower temperatures by performing off-beam
21
22 212 PC experiments, for which both longer run durations and excess water (i.e., water saturated) conditions
23
24 213 could be more easily achieved. For these experiments, the solid starting material was loaded together
25
26 214 with 10 wt.% deionized water in a gold capsule welded shut. This type of hydration conditions will be
27
28 215 referred to as *saturated* hereafter. Low-friction NaCl-based pressure cells (1/2 inch) were used. More
29
30 216 details on the pressure assembly can be found in Brunet et al. (2003). The temperature was measured
31
32 217 with an S-type thermocouple and regulated within 1 K with a Eurotherm™ controller.

33 218 Angle dispersive XRPD patterns were collected on quenched products with a Rigaku
34
35 219 diffractometer (Ultrax18hf-RINT2500) equipped with a Cu rotating anode (300 mA, 40 kV). XRPD data
36
37 220 were collected using 0.02° steps at a speed of 2°/min. In this case, the reaction extent, $\xi(t)$, could be
38
39 221 determined from reactant/product molar proportions in the quenched samples as follows. First, phase
40
41 222 proportions were calculated using the following relation:

$$42 \quad 223 \quad \frac{\chi_P}{\chi_B} = \varphi \frac{I_P}{I_B} \quad (3),$$

43 224
44
45 225

46
47 226 where φ is a constant, χ is the weight fraction of a given phase in the sample, I is the height (i.e.,
48
49 227 counts) of a selected diffraction peak, and the subscripts P and B stand for portlandite and brucite,
50
51 228 respectively. The value of φ was calibrated from mixtures of known portlandite to brucite weight
52
53 229 proportions using the height of the (001) reflection of each phase. The reaction progress, $\xi(t)$,
54
55 230 corresponding to the molar fraction of the forming phase, brucite, was then estimated from the
56
57 231 relation:

1
2
3
4 232
$$\frac{\xi}{1-\xi} = \frac{\chi_B M_B}{\chi_P M_P} \quad (4),$$

5
6 233

7 234 where M_P and M_B are the molar masses of portlandite and brucite, respectively.
8
9

10 235

11 12 236 **One-dimension diffusion experiments under *intermediate* hydration level** 13 14 237

15
16 238 The kinetics of Reaction (1) was further investigated in a one-dimension set-up using the piston-
17
18 239 cylinder apparatus (1D-PC experiments) by measuring the width of the reaction zone, which developed
19
20 240 at the interface between magnesite and portlandite polycrystals. This set-up aimed at characterizing
21
22 241 grain-boundary transport with the simplest geometry. Contrary to the kinetic experiments described in
23
24 242 the previous section, individual magnesite and portlandite powders (same material as for DIA and PC
25
26 243 experiments but unmixed) were loaded one after the other in a gold capsule. As much as possible, the
27
28 244 contact between these two materials was made planar (Figure 5a). No water was added to the capsule
29
30 245 nor was the sample dried beforehand. The hydration level can therefore be considered here as
31
32 246 *intermediate*. As for multi-anvil experiments, the run products of 1D-PC experiments were embedded in
33
34 247 epoxy, cut and hand polished with diamond paste. After carbon coating, these samples were also
35
36 248 characterized using the FE-SEM.

37 249 In order to investigate the temperature dependency of the chemical transport kinetics, these
38
39 250 experiments were performed in the 773–873 K temperature range. Typical reaction front widths of
40
41 251 ~ 1 mm were obtained for durations of a several days.
42
43 252

44 45 253 **EXPERIMENTAL RESULTS** 46 47 254

48 255 Bulk kinetic data from time-resolved XRD
49
50 256
51

52 257 In total, 16 experiments have been successfully performed on Reaction (1) with time-resolved
53
54 258 in-situ XRPD at 1.8 GPa and for temperatures ranging from 573 to 873 K (Table 2). It must be noted that
55
56 259 each dataset is composed of tens to hundreds of diffraction patterns, each represented by a data point
57
58 260 in left and middle panels of Figure 3. Water saturated conditions were investigated at two single
59
60

1
2
3 261 temperatures (393 and 423 K) through four and five PC experiments (Figure 3), respectively, which
4
5 262 therefore correspond to two kinetic data points for *saturated* conditions in Figure 4. Hundreds of PC
6
7 263 experiments would have been required to achieve a time resolution on the reaction progress similar to
8
9 264 that of the synchrotron-based experiments, which clearly emphasizes the advantage of using an in-situ
10
11 265 technique for kinetic purposes.

12
13 266 The scattering observed in the kinetic data obtained from synchrotron XRPD indicates a
14
15 267 precision of +/- 10% on the reaction progress (Figure 3). However, the precision on the reaction kinetics
16
17 268 is better owing to the averaging of the large number of data at each PT conditions. For PC experiments,
18
19 269 the precision on the determination of the reaction progress is expected to be better than 5%; in
20
21 270 particular, sample heterogeneity is averaged out by x-ray diffraction pattern collected on a larger
22
23 271 sample volume

24 272 As one can observe from the shape of the reaction curves, the reaction rate is the fastest when
25
26 273 the reaction starts and slows down as the reaction proceeds. Heterogeneous reactions, such as the one
27
28 274 studied here, do not generally comply with simple kinetic laws such as zero- or first-order. Furthermore,
29
30 275 the presence of a grain size distribution instead of single grain size in the starting material will influence
31
32 276 the shape of the kinetic curve if the reaction process is dependent on the reactive-surface area of the
33
34 277 reactants. Finally, change of hydration conditions from one set of experiments to another may lead to a
35
36 279 shape of the kinetic curves can be successfully fitted to an empirical Avrami law (Avrami, 1939) with an
37
38 280 exponent value of 0.4, which, according to Christian (1975), would reflect a diffusion limited reaction
39
40 281 process. However, due to the truly empirical character of these fits, following (Brown *et al.*, 1962), we
41
42 282 decided to merely compare half-reaction times (i.e., the time needed to reach $\xi = 0.5$) between all
43
44 283 datasets in order to grasp the effect of water as a whole on the reaction kinetics (Table 2, Figure 4). **Note**
45
46 284 **that for the particular case of the PC experiments performed with 10 wt.% water (water saturated**
47
48 285 **conditions), dissolution-precipitation process is expected to occur. However, aqueous species transport**
49
50 286 **rate – rather than dissolution rate – may well be the rate limiting process. Diffusivity of aqueous species**
51
52 287 **in bulk water is not within the scope of the present study. These “saturated” experiments should be**
53
54 288 **seen as representative of the water-excess experiments usually carried out in experimental petrology.**

55
56 289 Both series of experiments performed under *dry* and *intermediate* conditions seem to display an
57
58 290 Arrhenius-type behavior (i.e., the logarithm of half reaction times have a linear dependency to reciprocal
59
60 291 temperature) although, comparatively, experimental data obtained for an *intermediate* hydration level

1
2
3 292 are much more scattered (Figure 4). The dependency of the reaction kinetic with water content is likely
4
5 293 causing the important scattering observed in the *intermediate* dataset (see Discussion section). The
6
7 294 present results illustrate a drastic effect of water content on the kinetics. We note that similar half
8
9 295 reaction times (ca. 1 hour) were obtained at ~823, 648 and 423 K, for *dry*, *intermediate* and *saturated*
10
11 296 conditions, respectively, although the gap between *intermediate* and *dry* conditions seems to shrink
12
13 297 towards higher temperatures due to an apparently larger activation energy of the kinetic under *dry*
14
15 298 conditions.

16 299 **Chemical transport through the $\text{CaCO}_3 + \text{Mg}(\text{OH})_2$ reaction rims**

17 300
18
19
20 301 FE-SEM images of the recovered 1D-PC samples show mineral intergrowth in reaction zones
21
22 302 composed of $\text{Mg}(\text{OH})_2$ and CaCO_3 (Figure 5a). Energy dispersive spectrometry data collected with the FE-
23
24 303 SEM indicated that the Ca/Ca+Mg molar ratio remains constant and equal to 0.5 across the reaction
25
26 304 zones. In all of the DIA samples, partly reacted magnesite grains are surrounded by reaction rims (Figure
27
28 305 5b) within which the grain size of the reaction products is found to gradually increase from the
29
30 306 Ara+Bru | Mag to the Port | Ara+Bru interfaces. These reaction rims are composed of equimolar $\text{Mg}(\text{OH})_2$
31
32 307 (brucite) + CaCO_3 (aragonite) and show the same textural characteristics (grain size distribution,
33
34 308 symplectite intergrowth) as the reaction fronts in 1D-PC experiments. For 1D-PC and DIA experiments,
35
36 309 the grain size of the reaction products varies between 30 nm and a few μm (Figure 5d and 5e),
37
38 310 depending on temperature, water content and run duration. The constant stoichiometry
39
40 311 ($\text{CaO}/\text{H}_2\text{O} = \text{MgO}/\text{CO}_2 = 1$) throughout the reaction zones in both 1-D experiments and DIA samples,
41
42 312 implies the equality of Ca (CaO) and H (H_2O) fluxes through the Port | Ara+Bru interface. Similarly, the
43
44 313 Mg (MgO) and C (CO_2) fluxes must be identical through the Ara+Bru | Mag interface. In experiment
45
46 314 PC_180, a Pt chip was positioned at the interface between portlandite and magnesite. The Pt chip
47
48 315 (Figure 5a) remained at the Port | Ara+Bru interface in the course of the diffusion process. Its presence
49
50 316 at the interface appears to have hindered the transport of species from the Port | Ara+Bru interface to
51
52 317 the Ara+Bru | Mag interface, as indicated by the depression of the reaction front opposite to the Pt chip.
53
54 318 Therefore, CaO and H_2O are the mobile species in the system, whereas MgO and CO_2 remained
55
56 319 comparatively immobile. This conclusion is in line with the grain size gradient observed across the
57
58 320 reaction zones, where grains situated next to the Port | Ara+Bru interface formed first and are therefore
59
60 321 larger.

323 \bar{D}_{CaO} retrieval from 1D experiments

324

325 We showed in the previous section that the reaction zone growth in 1D-PC and DIA samples is
 326 controlled (i.e., limited) by the diffusion of CaO, assuming that H₂O diffusion is not limiting. The growth
 327 rate of the reaction zone (front or rim) depends on the molar flux of the limiting diffusing species, i.e.,
 328 J_{CaO} in the present case, perpendicular to the reaction zone. Let us consider the equimolar mix of
 329 brucite and aragonite as a single phase having an effective molar volume corresponding to V_r (Figure
 330 6a). In the planar geometry of our 1D-PC experiments, since each mole of CaO diffusing through the
 331 front results in the creation of one mole of said hypothetical phase, the growth rate of the reaction front
 332 thickness, ΔX , can be written:

333

$$334 \quad \frac{d\Delta x}{dt} = J_{CaO} V_r \quad (5),$$

335

336

337 According to the formalism developed by Fislser and Mackwell (1994), the first Fick's law for
 338 diffusion can be used to write the CaO flux across the reaction zone, J_{CaO} , as a function of the CaO
 339 chemical potential gradient, $d\mu_{CaO}/dx$, as follows:

340

$$341 \quad J_{CaO} = -\frac{D_{CaO} C_{CaO}}{RT} \frac{d\mu_{CaO}}{dx} \quad (6).$$

342

343 Fislser and Mackwel (1994) also showed that this latter expression can be integrated using the mean-
 344 value theorem, introducing the mean diffusion coefficient, \bar{D}_{CaO} , which represents the mean value for
 345 the diffusion across the reaction front or rim. The flux can then be written:

346

$$347 \quad J_{CaO} = -\frac{\bar{D}_{CaO} C_{CaO}}{RT} \frac{\Delta\mu_{CaO}}{\Delta x} \quad (7),$$

348

349 where $\Delta\mu_{\text{CaO}} = \mu'_{\text{CaO}} - \mu^0_{\text{CaO}}$ and therefore represents the chemical potential difference across the
 350 reaction zone.

351 Let us now consider the Ara+Bru | Mag interface, where, by definition, $x = \Delta x$ (Figure 6a). If we
 352 consider the equilibrium between MgCO_3 , the reaction products and the diffusing components, CaO and
 353 H_2O , we can write that:

$$\mu_{\text{MgCO}_3} + \mu'_{\text{CaO}} + \mu'_{\text{H}_2\text{O}} = \mu_{\text{Mg(OH)}_2} + \mu_{\text{CaCO}_3} \quad (8).$$

357 In addition, at $x = 0$, $\mu^0_{\text{CaO}} = \mu_{\text{Ca(OH)}_2} - \mu^0_{\text{H}_2\text{O}}$. Assuming that water activity is constant across the whole
 358 sample (due to supposedly faster diffusion kinetics), then $\mu^0_{\text{H}_2\text{O}} = \mu'_{\text{H}_2\text{O}}$. We can therefore write:

$$\mu'_{\text{H}_2\text{O}} = \mu_{\text{Ca(OH)}_2} - \mu^0_{\text{CaO}} \quad (9).$$

362 Finally, combining equations (8) and (9) gives:

$$\mu'_{\text{CaO}} - \mu^0_{\text{CaO}} = \mu_{\text{Mg(OH)}_2} + \mu_{\text{CaCO}_3} - \mu_{\text{MgCO}_3} - \mu_{\text{Ca(OH)}_2} \quad (10),$$

366 from which we find that $\Delta\mu_{\text{CaO}} = \Delta_R G$. In addition, it can be noticed that, in the present case $C_{\text{CaO}} \cdot V_r = 1$.
 367 The combination of (5) and (7) then yields:

$$\frac{d\Delta x}{dt} = - \frac{\bar{D}_{\text{CaO}}}{RT} \frac{\Delta_R G}{\Delta x} \quad (11).$$

370 We note here that the mean diffusion coefficient, \bar{D}_{CaO} , is an effective (i.e., apparent) diffusion
 371 coefficient, considering the brucite + aragonite aggregate in the reaction zone as a homogeneous
 372 diffusing medium. Effective and grain boundary diffusion coefficients are related to one another by a

1
2
3 373 ratio that depicts the shape and the volume fraction of grain boundaries available for intergranular
4 374 diffusion. For example, in the ideal case where grain boundaries are planar (i.e., devoid of tortuosity)
5 375 and parallel to the diffusion flux, the following relation applies (Brady, 1983):
6
7
8

9 376
10
11 377
$$\bar{D}^{GB} = \bar{D} \frac{2l}{\pi\delta} \quad (12),$$

12
13

14 378
15
16
17 379 where l is the distance separating the diffusion planes, i.e., the grain size (Figure 6a), and δ is the grain
18 380 boundary width. Since this latter parameter is virtually impossible to determine, most authors choose to
19 381 report the product of the grain boundary diffusivity \bar{D}^{GB} and the grain boundary width, δ . However,
20 382 during the diffusion process and the growth of reaction rims or fronts, l is not constant but obeys an
21 383 exponential grain growth law (Joesten, 1991):
22
23
24
25

26 384
27
28 385
$$l = (\rho t)^{1/n} \quad (13),$$

29
30

31 386
32
33 387 where ρ and n are the grain coarsening rate constant and exponent, respectively. Combining relations
34 388 (12) and (13) yields the expression:
35
36
37

38 389
39
40 390
$$\bar{D}^{GB} = \bar{D} \frac{2(\rho t)^{1/n}}{\pi\delta} \quad (14).$$

41
42

43 391
44
45 392 It has been shown indeed that the growth of reaction fronts limited by grain boundary diffusion is no
46 393 more proportional to the square root of time, but that it slows down further with time due to grain
47 394 coarsening, and therefore decreasing availability of grain boundaries (Gardes & Heinrich, 2011). In that
48 395 case, Δx is proportional to $(t^{1-1/n})^{1/2}$, where n is the grain coarsening exponent. Here, the combination of
49 396 Equations (11) and (14) gives the relation between rim thickness and time as a function of the grain
50 397 boundary diffusion coefficient:
51
52
53
54
55

56 398
57
58
59
60

$$\frac{d\Delta x}{dt} \Delta x = -\bar{D}^{GB} \delta \frac{\Delta_{RG}}{RT} \frac{\pi}{2\rho^n} t^{-\left(\frac{1}{n}\right)} \quad (15).$$

400

Integrating the above equation, noting that for $t = 0$ then $\Delta x = 0$, we obtain the relation:

402

$$\Delta x = \sqrt{\left(-\bar{D}^{GB} \delta \frac{\Delta_{RG}}{RT} \frac{\pi}{\rho^n} \left(\frac{n}{n-1}\right)\right) t^{\frac{n-1}{2n}}} \quad (16).$$

404

In the present case (see Appendix 1), the grain size of the reaction products was analyzed using SEM imaging to constrain the grain coarsening parameters, ρ and n . Relation (16) was then used to derive $\bar{D}^{GB} \delta$ from 1D-PC experiments (Table 2), where a planar geometry applies (Figure 6a).

Generally speaking, the presence of water may impact \bar{D}_{CaO} values by affecting any of the other parameters included in Equation (14), namely CaO mobility in the intergranular medium (i.e., \bar{D}_{CaO}^{GB}), grain boundary width and grain growth. This holds for experimentally grown coronae and for natural metamorphic reactions as well and since these latter parameters are difficult to estimate, one might also want to compare effective diffusivity values, \bar{D}_{CaO} . This approach was chosen by Carlson (2010), where Al effective diffusion coefficients were retrieved in the case of natural metamorphic coronae; it allows evaluating the overall effects of water content variations on the growth of reaction zones and visualizing how they affect metamorphic reaction kinetics in general.

416

\bar{D}_{CaO} retrieval from reaction coronae (spherical setting)

418

Similar to our 1D-PC experiments, SEM examination of the DIA samples evidenced that the reaction proceeds via the development of reaction rims around magnesite grains. This is nicely illustrated by the coronae observed around coarser residual magnesite grains in some samples (Figure 5b). The dimensions of these reaction rims can be used to calculate effective diffusion coefficients according to the model shown in Figure 6b. We note however that, in the initial setting (at $t = 0$), magnesite grains are not surrounded strictly by portlandite only, but rather by a mix of finer magnesite grains and portlandite. This may result in low Ca availability for diffusion and growth of the reaction

60

426 rims, which, in turn, implies that the diffusion values retrieved may be underestimated. Unfortunately, it
 427 is impossible to measure the impact of this bias on the values retrieved.

428 **The spherical setting implies that Equations (5) through (7) defined above in a planar setting no**
 429 **longer apply. We used the analytical solution given for a spherical geometry in Abart et al. (2009) that**
 430 **relates the rim dimensions and the bulk diffusion coefficient. This relation was modified in order to take**
 431 **grain coarsening for intermediate conditions into account; the dry case was treated assuming constant**
 432 **grain size in the rim (see next section and Appendix 1 for details).**

433 It should be noted that rim widths are determined from SEM images of sample sections which
 434 do not necessarily pass through the center of the imaged magnesite grains. This can introduce a
 435 measurement bias with apparently larger r_A/r_B ratios. Therefore, as much as possible, only rims with the
 436 lowest r_A/r_B ratio were used for the present determination (i.e., largest residual grains were
 437 preferentially picked). Additional errors may arise from the estimation of the inner and outer rim
 438 dimensions, r_B and r_A respectively (see Table 2). Errors on those measurements are of 0.1-0.3 μm (Table
 439 2). According to Equation (A5), $\bar{D}_{\text{CaO}}^{GB} \delta$ is proportional to the square of r_B/r_0 , which is accounted for by
 440 the error bars in the Arrhenius plot (Figure 7a).

441 Diffusivity values obtained for both 1D-PC and DIA (3D) experiments are listed in Table 2 and are
 442 reported in Figure 7a (empty symbols). We note that the intermediate data, retrieved from 1D-PC, and
 443 DIA experiments, although conducted over very different time scales, (i.e., a few hours and several days
 444 respectively) show a good consistency. Despite the uncertainties discussed above, the results clearly
 445 show a gap between dry and intermediate conditions, where comparable diffusivities are found at 823
 446 and 673 K, respectively.

447

448 Numerical extraction of diffusivity values from bulk reaction kinetics

449 The bulk reaction progress, $\xi(t)$, represents the molar fraction of magnesite (or portlandite)
 450 having reacted after a given run duration. At the scale of a single magnesite grain surrounded by
 451 portlandite, the reaction progress, $X(t)$, is related to the inner rim radius, r_b , as follows:

452

$$453 \quad X(t) = 1 - \frac{r_B^3}{r_0^3} = 1 - y^3 \quad (17)$$

454

455

456

457

458

459

460

1
2
3 454
4
5
6 455 If reaction rim growth is the limiting factor to the bulk reaction progress, then reaction kinetics
7
8 456 derived from in-situ diffraction should correspond to the magnesite rim growth kinetics (i.e., $X(t) =$
9
10 457 $\xi(t)$). However, the relation between $\xi(t)$ and $X(t)$ depends on the magnesite grain size distribution.
11
12 458 SEM images show that this distribution consists of a fine-grained fraction ($<1 \mu\text{m}$) along with coarser
13
14 459 grains, which size can be as large as several tens of microns. We assumed a log-normal grain size
15
16 460 distribution, typical of ground powders (Astrom, 2006, German, 2009, Sanchidrian *et al.*, 2012),
17
18 461 characterized by γ_0 and σ , which represent respectively the mean and the standard deviation of the
19
20 462 grain size natural logarithm. The grain size distribution was binned into 25 grain sizes with
21
22 463 corresponding proportions (p_i). Using, again, the analytical solution derived from Abart *et al.* (2009) in
23
24 464 Equation (A5), we could simulate reaction progress data, $X_i(t)$, for each grain size. Then kinetic curves
25
26 465 (i.e., $\xi(t)$), were obtained by calculating the weighted sum: $\sum_{i=1}^{25} p_i X_i(t)$ with $\sum_{i=1}^{25} p_i = 1$. For each
27
28 466 experimental data set, this approach was used to simulate kinetic data with varying values of $\bar{D}_{\text{CaO}}^{\text{GB}} \delta$.
29
30 467 The best fit to the experimental data was then obtained using a standard grid search algorithm and by
31
32 468 minimizing the absolute value of the difference between modeled and observed kinetic curves; this
33
34 469 method is also known as Least Absolute Deviations (LAD) method. The uncertainty on $\bar{D}_{\text{CaO}}^{\text{GB}} \delta$ introduced
35
36 470 by possible error on the initial grain size distribution is addressed in Appendix 2. It should be noted here,
37
38 471 that, as mentioned in the experimental section of the present study, the diffraction peak intensities
39
40 472 used to calculate reaction progress may not reflect the actual proportion of a phase in the sample at a
41
42 473 given time but may differ significantly. Based on observations of the standard deviation in our DIA
43
44 474 datasets, we inferred that this bias could result in errors of ± 0.05 on $\xi(t)$, which impacts the values of
45
46 475 $\bar{D}_{\text{CaO}}^{\text{GB}} \delta$ retrieved by a factor of 3 at most.

43 476 All 10 DIA experiments under *intermediate* conditions were used to estimate the mean grain
44
45 477 boundary diffusivity, $\bar{D}_{\text{CaO}}^{\text{GB}} \delta$, in this fashion. However, for some experiments performed under *dry*
46
47 478 conditions, the model failed to fit the experimental data satisfactorily. This can be explained by the
48
49 479 minor amount of grain growth involved in *dry* conditions (maximum grain sizes in the reaction rims are
50
51 480 typically no larger than tens of nanometers), which is therefore difficult to characterize (see appendix 1).
52
53 481 Alternatively, we chose to fit the *dry* datasets without integrated grain growth, i.e., by using the
54
55 482 analytical solution given in Abart *et al.* (2009), which allowed us to retrieve mean bulk diffusivity values,
56
57 483 \bar{D}_{CaO} . Values of grain boundary diffusion, $\bar{D}_{\text{CaO}}^{\text{GB}} \delta$, were then calculated using equation (12) and an
58
59 484 estimated grain size of $l = 120 \text{ nm}$, based on measurements made on two recovered samples (see
60

1
2
3 485 Appendix 1). The results are listed in Table 2 and, as a test of consistency between the bulk and the
4
5 486 microscopic datasets, both are reported on an Arrhenius plot in Figure 7a, along with $\bar{D}_{\text{CaO}}^{\text{GB}}\delta$ values from
6
7 487 the literature (Figure 7b). Test analysis of the retrieved diffusion values with varying grain growth
8
9 488 parameters, n and ρ , showed that the errors introduced by the estimation of these parameters are
10
11 489 negligible compared to other sources of errors (namely the initial grain size distribution and the
12
13 490 experimentally determined reaction progress).

14
15 491 For four experiments performed under *intermediate* conditions and two experiments performed
16
17 492 under *dry* conditions, diffusivities could be retrieved from both the microscopic approach and by
18
19 493 simulating kinetic curves (bulk approach). The largest difference observed between the two approaches
20
21 494 is of 1.33 log units. Although these differences seem significant at first sight, they are within the
22
23 495 uncertainties discussed above. In fact, the two datasets evidence a good consistency between the
24
25 496 microscopic (reaction rim and 1D diffusion fronts) and the macroscopic approaches, as highlighted by
26
27 497 the Arrhenius plot on Figure 7a.

28
29 498 A drastic difference is observed between *dry* and *intermediate* datasets, where similar values of
30
31 499 $\bar{D}_{\text{CaO}}^{\text{GB}}\delta$ are found at ~823 and 673 K, respectively, similar to the temperature gap observed when
32
33 500 comparing bulk reaction kinetics, i.e., half-reaction times (Figure 4). As for half-reaction times, the
34
35 501 diffusivity gap between *dry* and *intermediate* seems to shrink towards higher temperatures. The
36
37 502 activation energy returned by the Arrhenius fit in the *dry* case is $573 \pm 208 \text{ kJ.mol}^{-1}$, which is indeed
38
39 503 considerably larger than for the *intermediate* case ($291 \pm 29 \text{ kJ.mol}^{-1}$). But, in the former case, due to
40
41 504 the narrower temperature range investigated, the uncertainty returned is too large to allow any
42
43 505 assertion regarding its absolute value. Conclusively, although our results strongly suggest a larger
44
45 506 activation energy in the *dry* case, they do not entirely exclude the possibility that the activation energy
46
47 507 be the same in both cases (i.e., around 300 kJ.mol^{-1}).

48
49
50
51
52
53
54
55
56
57
58
59
60

509 DISCUSSION

511 Consistency between bulk and microscopic approaches

512 In order to investigate the effect of water on the $\text{MgCO}_3 + \text{Ca(OH)}_2 \rightarrow \text{Mg(OH)}_2 + \text{CaCO}_3$ reaction
513 at 1.8 GPa, we designed experiments where the starting material is composed of a grain size distribution
514 of the first reactant (i.e., magnesite with a log-normal distribution which includes grains $> 10 \mu\text{m}$)

1
2
3 515 reacting with a fine and homogeneous matrix of the second reactant (portlandite $\leq 1 \mu\text{m}$). We show
4
5 516 here that this starting material is suitable for the estimation of **mean** diffusion coefficients from time-
6
7 517 resolved in-situ XRPD provided (1) that significant reaction extents be achieved with sufficient XRD
8
9 518 sensitivity, (2) that the grain-size distribution of the reactants can be approximated and (3) that the
10
11 519 texture of the reacted samples can be characterized post-mortem. Obviously, the conventional
12
13 520 approach, which consists in measuring the growth rate of reaction rims remains more accurate for the
14
15 521 determination of diffusion coefficients. However, the in-situ approach can be appealing in some
16
17 522 instances since it allows fast collection of large datasets as required when investigating a range of
18
19 523 hydration levels (or a range of pressures) at various temperatures. One obvious limitation of our in-situ
20
21 524 approach with respect to the effect of hydration on reaction kinetics is the absence of **a** sealed container
22
23 525 in order to ensure constant water concentration over the whole run duration. For example, in the case
24
25 526 of the present brucite-bearing system at 1.8 GPa, this limitation implies that the reaction kinetics of
26
27 527 samples containing a few thousands of ppm water cannot be reasonably investigated at temperature
28
29 528 above ca. 950 K at the hour timescale (Gasc et al., 2011). The noble metal often used as container
30
31 529 material strongly absorbs the x-ray radiation and therefore alters the XRD signal intensity. The use of
32
33 530 titanium as capsule material (Chollet *et al.*, 2009) for synchrotron diffraction experiments dealing with
34
35 531 water-bearing systems clearly opens the way to the collection of in-situ XRD data under controlled and
36
37 532 constant water content.

38

39 533

40 534 **Role of the geometry of the intergranular medium**

41 535 It is important to note that, in the present diffusion dataset, the effect of water content is
42
43 536 potentially twofold. Water content will modify the chemistry of the intergranular medium and impact
44
45 537 the effective intergranular diffusivity (here $\bar{D}_{\text{CaO}}^{\text{GB}}$). The presence of water can also modify the geometry
46
47 538 of the diffusion paths through grain growth or by controlling the grain boundary width. The impact of
48
49 539 grain coarsening on kinetics via the reduction of the intergranular medium available for diffusion can be
50
51 540 of several orders of magnitude (Carlson & Gordon, 2004). Therefore, the effect of grain growth has been
52
53 541 taken into account by introducing a grain-growth rate law (Appendix 1). However, it can be argued that
54
55 542 the diffusivity gap between *dry* and *intermediate* conditions results from variations of the effective grain
56
57 543 boundary width, δ . According to Relation (14), identical Ca diffusivity would imply that δ is at least 2
58
59 544 orders of magnitude greater in *intermediate* than in *dry* conditions at 823 K. This seems huge in
60
545 comparison to what we know about grain boundary width at ambient pressure. **Although** the effective

1
2
3 546 grain boundary width **may be larger than** the structural grain boundary width, **even in the absence of**
4 **fluids (Marquardt *et al.*, 2011)**, in our *dry* conditions, **the effective boundary width** –which is the one of
5 547 **anhydrous aggregates– should not exceed significantly the structural boundary width**, generally
6 548 described as being equal to a few nanometers (Bons *et al.*, 1990, Farver *et al.*, 1994, Hiraga *et al.*, 1999,
7 549 Ricoult & Kohlstedt, 1983, (Marquardt *et al.*, 2011). On the other hand, studies of water-mineral
8 550 interface structures show that no more than two monolayers of water are adsorbed at the surface of
9 551 calcite grains with water being structured over a distance of approximately 15 Å (Cooke *et al.*, 2010,
10 552 Fenter & Sturchio, 2004). This implies that δ cannot vary by more than one order magnitude between
11 553 *dry* and *intermediate* conditions. Conclusively, even if intergranular diffusion may be enhanced by small
12 554 amounts of water through grain boundary widening, this effect alone cannot be responsible for the
13 555 tremendous differences observed between *dry* and *intermediate* cases, which are greater than two
14 556 orders of magnitude at the lowest temperatures of the present study (Figure 7a). As suggested by the
15 557 change in activation energy from *intermediate* to *dry* condition, we are likely documenting here water-
16 558 content dependent diffusion mechanisms, where cation mobility is enhanced by the presence of
17 559 absorbed water at the grain surfaces (i.e., in the grain boundaries). However, it is possible that even
18 560 minor amounts of water, such as it is the case here, enhance diffusivity not by widening grain
19 561 boundaries – therefore increasing the structural grain boundary width – but by creating locally
20 562 connected porosity (most likely in the form of tubules at triple junctions). This would result in an
21 563 increased effective grain boundary width, which no longer relates to the actual structural grain
22 564 boundary width; and the term intergranular diffusion should be preferred over grain boundary diffusion.
23
24
25
26
27
28
29
30
31
32
33
34
35
36
37

38 566 We note, however, that so far, there has been no systematic measurement of the grain
39 567 boundary width or structure evolution with increasing pressure. There is, therefore, a clear need for in-
40 568 situ experiments which investigate, for instance, how confining pressure affects transport properties.
41
42
43
44
45

46 570 **Water content and intergranular Ca-diffusion regimes**

47
48
49 571 The effect of water content on calcium transport (reaction rim growth) derived here is very
50 572 consistent, at least from a qualitative point of view, with recent work on Mg and Al intergranular
51 573 transport (Milke *et al.*, 2013; Gardés *et al.*, 2012; Carlson, 2010). In these studies, as in the present one,
52 574 the addition of small amounts of water, ≤ 1 wt.%, was reported to enhance intergranular diffusion by
53 575 several orders of magnitude, resulting in equal transport properties at temperatures lower by hundreds
54 576 of degrees. We note that in all cases the activation energies are reported to decrease significantly with
55
56
57
58
59
60

1
2
3 577 increasing water content. The present results are also in good agreement with the results of Gasc et al.
4
5 578 (2011), where, using a PC set-up that was open with respect to water, a drastic reduction of the
6
7 579 electrical conductivity of polycrystalline brucite was observed between samples dried in an oven at
8
9 580 393 K –possibly containing adsorbed water– and samples chemically dried by the addition of CaO. This
10
11 581 was also accompanied by an increase of the activation energy of the electrical conductivity from 84 to
12
13 582 106 kJ mol⁻¹. Similarly, the kinetics of the Ca(OH)₂ + MgCO₃ → CaCO₃ + Mg(OH)₂ exchange reaction,
14
15 583 which is also controlled by intergranular transport under the investigated PT conditions, showed a
16
17 584 strong positive dependency with water content from *dry* to *saturated* conditions (Figure 4).

18 585 In the present study, *dry* conditions were achieved using chemical drying, i.e., by **maintaining**
19
20 586 low water fugacity **in** the sample with a CaO/Ca(OH)₂ solid buffer. The notion of *dry* conditions may
21
22 587 appear somehow contradictory since the *dry* sample contains hydroxide phases. It should rather be
23
24 588 understood in the frame of diffusivity regimes (Farver & Yund, 1995), which were recently redefined by
25
26 589 Gardés et al. (2012) on enstatite and enstatite + forsterite reaction rims. These authors suggested that
27
28 590 four different regimes can be distinguished as a function of water content; the first regime
29
30 591 corresponding to conditions where grain boundaries are essentially anhydrous. The exchange of water
31
32 592 between brucite inner grains and grain boundaries observed by Gasc et al. (2011) precludes the
33
34 593 occurrence of anhydrous grain boundaries in the presence of brucite, as in the present study. Indeed,
35
36 594 Milke et al. (2013) showed that water content at the 10th of ppm level is sufficient to switch from
37
38 595 anhydrous to hydrous-like reaction textures in OPX reaction rims at 850-900°C. Hence, the *dry*
39
40 596 conditions obtained here with the addition of CaO cannot correspond to Regime 1 defined by Gardés et
41
42 597 al. (2012). In addition, the fact that our diffusion data show the least scattering in the *dry* case (Figures 4
43
44 598 and 7a) suggests that they are relevant to Regime 3, corresponding to hydrous saturated grain
45
46 599 boundary, rather than Regime 2 where diffusivity is expected to be strongly dependent of water
47
48 600 content. Regarding our *intermediate* conditions, although our approach suffers from undetermined
49
50 601 water content, the absorbed water on grain surfaces is estimated to represent 1 wt.% of the starting
51
52 602 material at most, a value that is close to the 0.5 wt.% threshold proposed by Gardés et al. (2012) for the
53
54 603 transition between Regimes 3 and 4 for anhydrous magnesium silicates. Besides, according to Gardés et
55
56 604 al. (2012), diffusivity variations with water content are also expected to be encountered in Regime 4,
57
58 605 where interconnected fluid channels start occurring. This is consistent with the scattering of our
59
60 606 diffusivity data in *intermediate* conditions, since the water content in the sample likely varied from one
607
608 607 experiment to the other due to variable hygrometric conditions and to partial water draining during the
609
610 608 experiment. In fact, it might not be fortuitous that the lowest temperature datapoint at 573 K

1
2
3 609 performed under *intermediate* conditions led to a significantly higher diffusivity value than its
4 counterparts. For this reason, and despite the low uncertainty returned, the (apparent) activation
5 610 energy for the *intermediate* conditions should be considered with caution.
6
7 611

8
9 612 Helpa et al. (2014) studied experimentally Mg and Ca diffusion in dolomite reaction rims but
10 could not distinguish whether GB or volume diffusion was the dominant process. Both studies were
11 613 performed in anhydrous conditions and their results are compared to ours in Figure 7b. Extrapolation of
12 614 the Ca diffusion coefficients obtained in *dry* conditions to the 750-800°C temperature range indicates
13 615 that we found higher diffusivity by four and six orders of magnitude than Helpa et al. (2014) and Farver
14 616 and Jund (1996), respectively. This apparent discrepancy can be accounted for by different water
15 617 conditions investigated by these authors, which likely corresponded to Regime 1 (anhydrous) whereas
16 618 we interpreted our *dry* experiments as reflecting diffusional Regime 3 defined by Gardés et al. (2012).
17 619 For comparison, we also plotted on Figure 7b, the data on Mg diffusion in enstatite rims by Gardés et al.
18 620 (2012) and Gardés and Heinrich (2011) who respectively investigated Regime 3 and Regime 1. It can be
19 621 seen that differences of, at least, 6 orders of magnitude are encountered at 800°C between these two
20 622 diffusional regimes for $\bar{D}_{MgO}^{GB} \delta$. This comparison with Mg diffusivity in enstatite rims confirms that our
21 623 *dry* conditions are consistent with Regime 3.
22
23 624

24
25 625 Interestingly, a major difference between our results and the ones of Helpa et al. (2014) is the
26 626 unilateral aspect of the diffusion in our case, where Mg immobility is evidenced, whereas both species
27 627 (Mg and Ca) are found to diffuse at comparable rates in the experiments of Helpa et al (2014). The
28 628 difference is even more notable when comparing to the Mg-Ca-Si system, where it has been established
29 629 that Mg is the most mobile specie (Joachim *et al.*, 2011, Joachim *et al.*, 2012). Although these
30 630 differences are admittedly difficult to interpret in terms of diffusion mechanisms, it may well be related
31 631 to the fact that, in our particular case, Ca diffuses jointly with H₂O, associated to the breakdown of
32 632 portlandite upon reaction, which could, in turn, result in faster Ca mobility, relative to Mg.
33
34

35
36 633 Oxygen diffusivity in grain boundary of hot-pressed calcite aggregates was investigated by
37 634 Farver and Jund (1998) under hydrous conditions (Regime 3). As shown on Figure 7b, the corresponding
38 635 $D^{GB} \delta$ values for oxygen under these water conditions lie around our Ca diffusion data under *intermediate*
39 636 conditions.
40
41

42
43 637 One of the most striking feature of Figure 7b is the location of the Mg intergranular high-
44 638 temperature diffusivity data (0.1-0.5 and 5 wt.% H₂O, i.e., Regime 3 and 4, respectively) derived by
45
46
47
48
49
50
51
52
53
54
55
56
57
58
59
60

1
2
3 639 Gardés et al. (2012). Despite the addition of water, these data lie on the very slow diffusion side of the
4
5 640 plot, relatively close to the data for Ca diffusion in anhydrous carbonates (Farver and Yund, 1996; Helpa
6
7 641 et al., 2014) and far from hydrous Ca and O diffusion data in carbonates (this study and Farver and Jund,
8
9 642 1996, respectively). We believe that this discrepancy does not rely on the element/oxide that is
10
11 643 considered (Mg vs. Ca/O) in these studies but rather on the mineralogical/chemical system that was
12
13 644 investigated: silicate on the one side and CaCO₃ (Farver and Yund, 1994, 1996), CaMg(CO₃)₂ (Helpa et al.,
14
15 645 2014) or CaCO₃-Mg(OH)₂ (this study) on the other side. **In the case of volume diffusion, such differences**
16
17 646 **were already pointed out by Farver (1994), who showed that oxygen self-diffusion in non-silicates such**
18
19 647 **as magnetite, apatite and calcite, is more than two orders of magnitude larger than in silicates with the**
20
21 648 **same total ionic porosity. In the present case,** it is very likely that the hydrated brucite surfaces provide a
22
23 649 faster diffusion medium than the silicate ones in Gardés et al. (2012), the hydrophobic surface of which
24
25 650 likely favors the formation of water pores even at the 10th of ppm water content level (e.g., Milke et al.,
26
27 651 2013). However, in this case, one would expect their experiments performed in Regime 4, with
28
29 652 saturated hydrous grain boundaries, to yield diffusion coefficients similar or close to ours, which is far
30
31 653 from true, as shown by the data point corresponding to 1 wt.% of water from Gardés et al. (2012) in
32
33 654 Figure 7b. One major aspect one has to keep in mind when comparing these results is that, unlike for
34
35 655 self-diffusion experiments, the diffusion mechanism, here, as well as in Gardés et al. (2012), is driven by
36
37 656 a chemical reaction, as shown by the presence of the ΔG term in our Equations (16) and (A5) or in
38
39 657 Equations (1), (2) and (3) of Gardés et al. (2012). Now, the GB diffusivity contrast between our
40
41 658 experiments and those of Gardés et al. (2012) implies a huge gap between the temperatures required to
42
43 659 achieve measurable reaction rims at laboratory timescale (400°C vs. 1000°C, respectively). We believe
44
45 660 that this highlights the generally well known difference between reaction kinetics in silicate and
46
47 661 carbonate systems, which is often expressed in terms of dissolution rates contrast between rather
48
49 662 soluble carbonates and less soluble silicates (Dolejs and Manning (2010) and references therein). In
50
51 663 nature, **when intergranular fluids are present and transport is no longer limiting,** these solubility
52
53 664 differences tend to control the kinetics of metamorphic equilibration (Carlson *et al.*, 2015). We show
54
55 665 here that the kinetic contrast between the silicate and carbonate systems seems to hold at very low
56
57 666 water contents and even under *dry* conditions. As a consequence, although the drastic effect of low
58
59 667 water content (< 1 wt.%) on intergranular diffusion in mineral aggregates can be understood in the
60
61 668 frame of water sensitive diffusional regimes (Rubie, 1986; Farver and Jund, 1995; Carlson, 2010, Gardés
62
63 669 et al., 2012), substantial intergranular diffusivity variations will depend on the chemical and physical
64
65 670 properties of intergranular media, which may drastically differ in laboratory experiments and in Nature.

671

672 **Implications for metamorphism**

673 The need for short run duration imposed by the synchrotron beam availability led us to focus on
674 a system characterized by relatively high reaction kinetics, even under *dry* conditions. Consequently, our
675 experiments significantly departed from nature-relevant kinetics, where slow diffusing species such as Al
676 control the reaction rate. Our conclusions on the effect of water content are, however, in line with those
677 from Carlson (2010) who, based on natural metamorphic reaction coronae, showed that large gaps exist
678 between aluminum grain boundary diffusivities under “nearly anhydrous” and “hydrous but fluid-
679 undersaturated” conditions. Carlson (2010) also suggested an increase of the activation energy of the
680 diffusion from fluid-saturated to anhydrous conditions. Furthermore, it seems that another large
681 diffusivity gap exists as the water content increases and the fluid phase becomes interconnected
682 (Brenan, 1993). Considering now the recent study by Gardés et al. (2012), which depicts the same type
683 of picture, it seems that a general scheme arises with a set of diffusivity regimes controlled by water
684 content.

685 A central question with respect to natural systems is whether water content will affect
686 metamorphic reactions in the temperature range at which they occur. Indeed, the decrease of the
687 activation energy of the diffusion with increasing water content, suggests that reaction kinetics are
688 unaffected by water content above a given temperature. In our case, the temperature corresponding to
689 the intersection between the Arrhenius laws determined under *dry* and *intermediate* conditions lies at
690 ~ 1600 K. For both the data reported by Carlson (2010) and Gardés et al. (2012), **this** intersection is
691 found at even higher temperature values. It is therefore likely that the strong effect of water activity
692 (even when < 1) on reaction kinetics reported here will be relevant to most metamorphic conditions.

693 In high-grade lower crustal rocks, water activity is mostly expected to be below unity (e.g.,
694 Yardley and Valley, 1997) and, therefore, aside from Regime 4, the various diffusivity regimes re-defined
695 by Gardés et al. (2012) can potentially operate. In dry lower-crustal rocks, when hydrous silicates are still
696 present, for example, water activity is close to 10^{-2} (Yardley and Valley, 1997), this corresponds to what
697 we called *dry* conditions here and tentatively interpreted as saturated (or partly saturated) grain
698 boundaries, although in the absence of free fluids. Even if our understanding of intergranular transport
699 in water undersaturated rock is still very poor, our experiments show that, in lower crustal rocks, grain
700 boundary diffusion rates are rendered much faster by the simple presence of hydrous phases such as

1
2
3 701 brucite. Furthermore, since the addition of minor amounts of water are sufficient to allow transition
4
5 702 from Regime 3 to 4, mineral reaction rates are prone to vary by several orders of magnitude with
6
7 703 relatively small changes in water activity. It can therefore be emphasized that, as much as temperature,
8
9 704 water activity is a first order parameter that will control reaction rates among minerals. In water-bearing
10
11 705 rocks – meaning here rocks which are not anhydrous – the effect of increasing temperature on grain
12
13 706 boundary diffusivity will be enhanced by structural water contained in hydrous minerals being
14
15 707 progressively transferred into grain boundaries, e.g., Gasc et al. (2011) for a laboratory case and Hetenyi
16
17 708 et al. (2007) for a natural case.

18 709

For Peer Review

1
2
3 710 **APPENDIX 1: Estimation of grain coarsening parameters and implementation in the analytical**
4
5 711 **solution of Abart et al. (2009) for a spherical geometry.**
6

7 712 Sample PC175 which was **obtained** under intermediate conditions **exhibits** the largest reaction
8
9 713 front, which allows the most precise characterization of grain growth among our samples.
10
11 714 Measurements of grain size across the reaction front showed that it is proportional to the distance from
12
13 715 the Ara+Bru | Mag interface, where the products nucleate (Figure A1).
14

15 716 This implies that the grain size of the products is proportional to the reaction front width, **i.e.**
16
17 717 $l \propto \Delta x$. Since PC175 is a 1-D diffusion experiment, we can consider the relation defined by Gardés and
18
19 718 Heinrich (2011) where reaction front growth controlled by grain boundary diffusion obeys:
20

21 719
22 720
$$\Delta x = A\sqrt{t^{1-1/n}} \quad (A1)$$

23
24 721

25
26 722 and where A is a constant, and n is the grain growth exponent. At a given temperature, grain growth is
27
28 723 known to have an exponential dependence with time of the form
29

30 724
31 725
$$l = (\rho t)^{1/n} \quad (A2),$$

32
33 726

34 727 where ρ is the growth rate constant. **Proportionality between grain size** and Δx whatever t implies that
35
36 728 $\frac{1-1/n}{2} = 1/n$, i.e, $n = 3$. Note that this is the value of n that is used in Gardés and Heinrich (2011). Then,
37
38 729 assuming a value of $n = 3$ for **intermediate conditions**, ρ could be retrieved **for experiments where SEM**
39
40 730 **images allowed** measuring the maximum grain size, l , of the products; and using Equation (A2). **This was**
41
42 731 **done** for six **intermediate** and two **dry** conditions experiments, respectively. **However, under dry**
43
44 732 **conditions, grain growth is limited, with final grain sizes that never exceed 150 nm. In addition, the**
45
46 733 **nucleus size of the reaction products in the reaction rim is unknown. Grain growth in dry conditions was**
47
48 734 **therefore neglected without inducing significant error on the retrieved diffusion values.**

49 735 The temperature dependency of ρ is of Arrhenius type:
50

51 736
52
53 737
$$\rho = \rho_0 \times \exp\left[-\frac{Q}{RT}\right] \quad (A3),$$

54
55 738

with $Q = 274 \text{ kJ mol}^{-1}$ and $r_0 = 6.85 \times 10^{-5} \text{ m}^{1/3} \text{ s}^{-1}$ for the *intermediate* dataset (Fig. A2). Using relation (A3), ρ could be calculated for all DIA experiments run under *intermediate* conditions and further used to calculate the corresponding $\bar{D}_{\text{CaO}}^{\text{GB}} \delta$ product as described in the Results section.

In order to use the grain coarsening model above to retrieve $\bar{D}_{\text{CaO}}^{\text{GB}} \delta$ in the spherical geometry, differential equation (32) in Abart et al. (2009) has been modified to yield the following integral form:

$$\int_1^y y \left(\frac{y}{(1+u(y^3-1))^{1/3}} - 1 \right) dy = -\bar{D}_{\text{CaO}}^{\text{GB}} \delta \frac{\Delta_r G V_m}{RT V_r} \frac{\pi}{2r_0^2 \rho^{1/n}} \int_0^t t^{-\frac{1}{n}} dt \quad (\text{A4})$$

Noting that $y = 1$ for $t = 0$, we obtain the relation between grain boundary diffusivity, time and rim dimensions for a spherical geometry:

$$\frac{1-y^2}{2} - \frac{1}{2u} \left\{ 1 - [1 + u(y^3 - 1)]^{2/3} \right\} = -\bar{D}_{\text{CaO}}^{\text{GB}} \delta \frac{\Delta_r G V_m}{RT V_r} \frac{\pi}{2r_0^2 \rho^{1/n}} \frac{n}{n-1} t^{\frac{n-1}{n}} \quad (\text{A5})$$

$$\text{where } y = \frac{r_B}{r_0}.$$

Equation (A5) was used to calculate grain boundary diffusion coefficients based on measurements of r_A and r_B (Figure 6b). However, using this solution implies calculating first the position of the initial interface r_0 . The position of r_0 relative to r_A and r_B can be found assuming that one mole of portlandite (i.e., $\text{CaO} + \text{H}_2\text{O}$) entering the rim, yields one mole of reaction products, $n_M = n_r$, where, again, the brucite + aragonite assemblage is considered as a single phase with a molar volume V_r that is the sum of brucite and aragonite individual molar volumes. We note that, at any time, the volume of a magnesite grain having reacted corresponds to $n_M V_M = \frac{4}{3} \pi (r_0^3 - r_B^3)$. Similarly, we can write that the volume of the reaction products corresponds to the volume of the rim, $n_p V_r = \frac{4}{3} \pi (r_A^3 - r_B^3)$. As stated above, the equality between the number of moles on each side, leads to the relation:

$$\frac{V_M}{V_r} = \frac{r_0^3 - r_B^3}{r_A^3 - r_B^3} \quad (\text{A6})$$

The r_0 values were therefore calculated using Equation (A6) and then used to retrieve $\bar{D}_{\text{CaO}}^{\text{GB}} \delta$ values with Equation (A5).

1
2
3 7644
5 765 **APPENDIX 2: Dependency of diffusivity data on the input grain size distribution**6
7 766 The distribution of the initial magnesite grain size in our model impacts the diffusion coefficient
8 767 retrieved, simply because finer grains tend to react faster than their coarser counterparts. Although the
9 768 initial grain size distribution was partly characterized by SEM images, the consistency between the two
10 769 parameters that control the grain size distribution, γ_0 and σ , and the actual magnesite grains dimensions
11 770 was tested by a series of simulations. This also allowed us to estimate the errors resulting from
12 771 approximations made on the aforementioned grain size distribution.13
14 772 In the log-normal distribution, γ_0 represents the natural logarithm of the median value, which,
15 773 based on SEM characterization, was set to 2 μm . The impact of γ_0 on diffusivity was tested for values
16 774 varying from $\exp(\gamma_0) = 1-5 \mu\text{m}$. In the investigated range, the retrieved $\bar{D}_{\text{CaO}}^{\text{GB}}\delta$ values vary almost
17 775 linearly with γ_0 (from 1.66×10^{-24} to $4.94 \times 10^{-23} \text{ m}^3\text{s}^{-1}$ for experiment X11, for example). The parameter
18 776 σ is also critical since it impacts the proportion of large grains present in the sample; it was estimated
19 777 based on SEM images, which show that large grains, coarser than 20 μm , represent ~30% of the whole
20 778 magnesite initial volume. This is best modeled with $\sigma = \ln(2.5)$. However, we considered here that the
21 779 uncertainty resulting from the error on σ corresponds to $2.2 < \exp(\sigma) < 2.9$, which translates into a
22 780 volume percentage of large grains comprised between ~10 to 50 %. We remind that this error does not
23 781 represent an actual variation of grain size distribution in the starting material but rather the amount of
24 782 large grains sampled by the X-ray beam –therefore contributing to the overall kinetic. This may vary due
25 783 to poor statistics, i.e. a handful of large grains only could result in an apparently slower kinetic, and, in
26 784 the contrary, if little to no large grains are present, kinetic will appear faster, as it will be mainly
27 785 controlled by the reaction of small grains. The results of these tests show that, for experiment X11 for
28 786 example, when $\exp(\sigma)$ varies from 2.2 to 2.9, the obtained values of $\bar{D}_{\text{CaO}}^{\text{GB}}\delta$ vary from 2.80×10^{-24} to
29 787 $2.25 \times 10^{-23} \text{ m}^3\text{s}^{-1}$. It should be noted here, that we expect the grain size distribution in the starting
30 788 material to be similar in all experiments and, therefore, errors discussed above should not affect the
31 789 variations of $\bar{D}_{\text{CaO}}^{\text{GB}}\delta$ observed upon water content and temperature.32
33
34
35
36
37
38
39
40
41
42
43
44
45
46
47
48
49
50
51 790

1
2
3 791 **ACKNOWLEDGEMENTS**
4

5
6 792 Univ. Paris-XI funded JG PhD grant. Financial support through PROCOPE (grant 09383RJ), HASYLAB and
7 793 SYSTER (CNRS-INSU) is acknowledged. We are indebted to E. Gardés, W. Carlson and an anonymous
8
9 794 reviewer for very constructive reviews that greatly improved the manuscript. The authors thank G.
10
11 795 Hetényi, D. Daval and A. Fernandez-Martinez for valuable discussions.
12
13
14
15
16
17
18
19
20
21
22
23
24
25
26
27
28
29
30
31
32
33
34
35
36
37
38
39
40
41
42
43
44
45
46
47
48
49
50
51
52
53
54
55
56
57
58
59
60

For Peer Review

796 **FIGURE CAPTIONS**

797
798 **Figure 1:** XRPD patterns collected on sample Y13 showing the early water activity buffering of the lime
799 (LIM) – portlandite (POR) pair upon heating at 1.8 GPa. MAG, BRU, CAL and ARA stand for
800 magnesite, brucite, calcite and aragonite, respectively. The grey and black patterns correspond to data
801 collected at room temperature and shortly before the target temperature of 833 K was reached,
802 respectively. Note that most peaks are shifted towards lower energies upon heating due to thermal
803 expansion. At ca. 833 K upon heating, small amounts of reaction products, i.e., brucite and aragonite, are
804 present along with minor transient calcite. The persistence of CaO is evidenced by its (200) reflection at
805 33.85 keV (black pattern), the intensity of which drastically decreased upon heating, as shown by the
806 comparison between the grey and black diffraction patterns, then remained constant during the rest of the
807 experiment. The partial consumption of CaO is interpreted as resulting from the reaction with the
808 sample/assembly water to form Ca(OH)₂. Numbers in parentheses are Miller indices of the diffracting
809 planes.
810

811 **Figure 2:** In-situ XRPD data for Reaction (1) under *intermediate* conditions at 573 K and 1.8 GPa (run
812 X15). The spectra were collected with a step time of 45 s. The main diffraction peaks are indexed,
813 including reflections used for the calculation of reaction progress and the BN reflection used for intensity
814 normalization. Note that the corresponding diffraction energies differ from Figure 1 due to a different
815 angle of the detector relative to the incident beam.
816

817 **Figure 3:** Bulk kinetic data (reaction progress) and simulated kinetic curves. (a) *Dry* conditions (DIA);
818 (b) *Intermediate* conditions (DIA); (c) *Saturated* conditions (PC). Reaction progress data were obtained
819 from diffraction reflections relative intensities for (a) and (b) (see text for details) and from Equation (4)
820 for (c).
821

822 **Figure 4:** Half-reaction times obtained from all 16 DIA experiments as well as from the two sets of PC
823 experiments, at 393 K and 423 K. Values are plotted on a logarithmic scale vs. reciprocal temperature.
824 Usual time measures are given as a guide to apprehend the tremendous effect of temperature on the
825 kinetics, which range from seconds to weeks within less than a 200-degree span. Triangles, diamonds and
826 circles stand for *dry*, *intermediate* and water *saturated* conditions, respectively.
827

828 **Figure 5:** FE-SEM images in back-scattered electrons (BSE) mode of recovered samples. Abbreviations
829 Por, Mag, Bru and Ara stand for portlandite, magnesite, brucite and aragonite respectively. (a) 1D-PC
830 sample PC180. The reaction front between Portlandite (lower, bright phase) and MgCO₃ (upper dark
831 phase) is visible. The Pt chip (white color) is at the Port | Ara+Bru interface. The fracture network formed
832 upon sample decompression and was not present when the sample reacted. (b) and (c) DIA samples Y10
833 and Y11, respectively. After collection of the kinetic data (shown in Figure 3) the temperature was
834 increased for both samples to ~1073 K (see experimental section for details). (b) As a result these samples

1
2
3 835 show large reaction rims around the coarsest residual magnesite grains. (c) Also thanks to higher
4 836 temperatures, nicely defined palisade-type rims with brucite and aragonite (darker and brighter phases,
5 837 respectively) intergrowths are observed. The edge of a residual magnesite grain is visible in the lower left
6 838 corner. (d) and (e) Detailed views of a reaction rim in samples AA13 and AA10, respectively. The
7 839 reacting magnesite grain is visible in the bottom lower corner in both cases. Note the finer grain size of
8 840 the reaction products in (e), due to a lower temperature.
9
10 841

11
12
13 842 **Figure 6:** Idealized geometries taken for the calculation of $\bar{D}_{\text{CaO}}^{\text{GB}}\delta$. (a) Planar geometry used for
14 843 calculations of diffusion coefficients from reaction front thickness (1D-PC experiments). (b) Spherical
15 844 geometry used for the calculation of $\bar{D}_{\text{CaO}}^{\text{GB}}\delta$ from reaction rim dimensions (DIA experiments, microscopic
16 845 approach) and using the analytical solution derived from Abart et al. (2009) to fit the kinetic curves (DIA
17 846 experiments, macroscopic approach).
18
19

20 847
21
22 848 **Figure 7:** Summary of the $\bar{D}_{\text{CaO}}^{\text{GB}}\delta$ values obtained in this study and comparison with literature data. (a)
23 849 Triangles and squares correspond to *intermediate* and *dry* data, respectively. Empty symbols represent
24 850 values retrieved from SEM measurements of reaction rim widths for both *intermediate* and *dry* conditions
25 851 (microscopic approach) with down-pointing triangles representing the 1D-PC data obtained under
26 852 *intermediate* conditions. Diffusion data extracted from reaction progress vs. time curves are reported with
27 853 filled symbols (bulk approach). The dashed lines represent Arrhenius laws obtained by least square fitting
28 854 of the *dry* and *intermediate* data; the activation energies and their respective uncertainties obtained are
29 855 also labelled. (b) The Arrhenius laws corresponding to our data and shown on (a) are also reported here
30 856 (same dashed lines) along with grain boundary diffusion data from the literature regarding carbonates:
31 857 Farver and Yund (1996), Ca diffusion in calcite (empty diamonds); Farver and Yund (1998), O diffusion
32 858 in calcite (filled diamonds); Helpa et al. (2014), Ca diffusion during dolomite rim growth (empty stars).
33 859 Additional data were added to illustrate previously demonstrated effect of water content: the black and
34 860 grey curves and the circle represent diffusion regimes 1, 3 and 4 of Mg in enstatite grain boundaries, as
35 861 defined in Gardés and Heinrich (2011) and Gardés et al. (2012); these correspond to dry conditions and
36 862 0.1-0.5 wt.% and 2.1 wt.% water, respectively.
37
38
39
40
41 863

42
43 864 **Figure A1:** Grain size of the reaction products across the reaction front in sample PC175. Grain sizes
44 865 correspond to the average measurement of the five largest identified grains in each location. An SEM
45 866 backscattered electron image of the reaction front is superimposed to illustrate the grain size gradient.
46 867

47
48 868 **Figure A2:** Arrhenius plot showing the values of ρ obtained from grain size measurements at various
49 869 temperatures for *intermediate* and *dry* experiments (circles and squares, respectively). The linear
50 870 regression shown by the dashed line returned the values indicated in the adjacent box, according to
51 871 equation (A3), with Q in J mol^{-1} .
52

53 872

54 873

55

56

57

58

59

60

874 REFERENCES

- 875 Abart, R., Petrishcheva, E., Fischer, F. D. & Svoboda, J. (2009). Thermodynamic model for diffusion
876 controlled reaction rim growth in a binary system: application to the forsterite-enstatite-quartz system.
877 *American Journal of Science* **309**, 114-131.
- 878 Astrom, J. A. (2006). Statistical models of brittle fragmentation. *Advances in Physics* **55**, 247-278.
- 879 Austrheim, H. (1987). Eclogitization of lower crustal granulites by fluid migration through shear zones.
880 *Earth and Planetary Science Letters* **81**, 221-232.
- 881 Avrami, M. (1939). Kinetics of phase change I - General theory. *Journal of Chemical Physics* **7**, 1103-
882 1112.
- 883 Baxter, E. F. (2003). Natural constraints on metamorphic reaction rates. In: Vance, D., Muller, W. &
884 Villa, I. M. (eds.) *Geochronology: Linking the Isotopic Record with Petrology and Textures*. Bath:
885 Geological Soc Publishing House, 183-202.
- 886 Berman, R. G. & Aranovich, L. Y. (1996). Optimized standard state and solution properties of minerals
887 .1. Model calibration for olivine, orthopyroxene, cordierite, garnet, ilmenite in the system FEO-MGO-
888 CaO-Al₂O₃-TiO₃-SiO₂. *Contributions to Mineralogy and Petrology* **126**, 1-24.
- 889 Bons, A. J., Drury, M. R., Schryvers, D. & Zwart, H. J. (1990). The nature of grain-boundaries in slates -
890 implications for mass-transport processes during low-temperature metamorphism. *Physics and Chemistry*
891 *of Minerals* **17**, 402-408.
- 892 Brady, J. B. (1983). Intergranular diffusion in metamorphic rocks. *American Journal of Science* **283**, 19.
- 893 Brenan, J. M. (1993). Diffusion of chlorine in fluid-bearing quartzite - effects of fluid composition and
894 total porosity. *Contributions to Mineralogy and Petrology* **115**, 215-224.
- 895 Brown, W. H., Fyfe, W. S. & Turner, F. J. (1962). Aragonite in california glaucophane schists, and the
896 kinetics of the aragonite-calcite transformation. *Journal of Petrology* **3**, 566-&.
- 897 Brunet, F., Bagdassarov, N. & Miletich, R. (2003). Na₃Al₂(PO₄)₃, a fast sodium conductor at high
898 pressure: in-situ impedance spectroscopy characterisation and phase diagram up to 8 GPa. *Solid State*
899 *Ionics* **159**, 35-47.
- 900 Carlson, W. D. & Gordon, C. L. (2004). Effects of matrix grain size on the kinetics of intergranular
901 diffusion. *Journal of Metamorphic Geology* **22**, 733-742.
- 902 Carlson, W. D. (2010). Dependence of reaction kinetics on H₂O activity as inferred from rates of
903 intergranular diffusion of aluminium. *Journal of Metamorphic Geology* **28**, 735-752.
- 904 Carlson, W. D., Hixon, J. D., Garber, J. M. & Bodnar, R. J. (2015). Controls on metamorphic
905 equilibration: the importance of intergranular solubilities mediated by fluid composition. *Journal of*
906 *Metamorphic Geology* **33**, 123-146.
- 907 Chollet, M., Daniel, I., Koga, K. T., Petitgirard, S. & Morard, G. (2009). Dehydration kinetics of talc and
908 10 angstrom phase: Consequences for subduction zone seismicity. *Earth and Planetary Science Letters*
909 **284**, 57-64.
- 910 Christian, J. W. (1975). Theory of transformations in metals and alloys. I. Equilibrium and general kinetic
911 theory, 2nd edition. *Theory of transformations in metals and alloys. I. Equilibrium and general kinetic*
912 *theory, 2nd edition*, xvi+586 pp-xvi+586 pp.

- 1
2
3 913 Cooke, D. J., Gray, R. J., Sand, K. K., Stipp, S. L. S. & Elliott, J. A. (2010). Interaction of Ethanol and
4 914 Water with the {1014} Surface of Calcite. *Langmuir* **26**, 14520-14529.
- 5 915 Decker, D. L. (1971). High-pressure equation of state for NaCl, KCl, and CsCl. *Journal of Applied*
6 916 *Physics* **42**, 3239-&.
- 7 917 Dolejs, D. & Manning, C. E. (2010). Thermodynamic model for mineral solubility in aqueous fluids:
8 918 theory, calibration and application to model fluid-flow systems. *Geofluids* **10**, 20-40.
- 9 919 Farver, J. R. (1994). OXYGEN SELF-DIFFUSION IN CALCITE - DEPENDENCE ON
10 920 TEMPERATURE AND WATER FUGACITY. *Earth and Planetary Science Letters* **121**, 575-587.
- 11 921 Farver, J. R. & Yund, R. A. (1995). Grain-boundary diffusion of oxygen, potassium and calcium in
12 922 natural and hot-pressed feldspar aggregates. *Contributions to Mineralogy and Petrology* **118**, 340-355.
- 13 923 Farver, J. R. & Yund, R. A. (1996). Volume and grain boundary diffusion of calcium in natural and hot-
14 924 pressed calcite aggregates. *Contributions to Mineralogy and Petrology* **123**, 77-91.
- 15 925 Farver, J. R. & Yund, R. A. (1998). Oxygen grain boundary diffusion in natural and hot-pressed calcite
16 926 aggregates. *Earth and Planetary Science Letters* **161**, 189-200.
- 17 927 Farver, J. R., Yund, R. A. & Rubie, D. C. (1994). Magnesium grain-boundary diffusion in forsterite
18 928 aggregates at 1000-degrees-1300-degrees-C and 0.1-MPa TO 10-GPa. *Journal of Geophysical Research-*
19 929 *Solid Earth* **99**, 19809-19819.
- 20 930 Fenter, P. & Sturchio, N. C. (2004). Mineral-water interfacial structures revealed by synchrotron X-ray
21 931 scattering. *Progress in Surface Science* **77**, 171-258.
- 22 932 Fisler, D. F. & Mackwell, S. J. (1994). Kinetics of diffusion-controlled growth of fayalite. *Physics and*
23 933 *Chemistry of Minerals* **21**, 156-165.
- 24 934 Gardés, E. & Heinrich, W. (2011). Growth of multilayered polycrystalline reaction rims in the MgO-SiO₂
25 935 system, part II: modelling. *Contributions to Mineralogy and Petrology* **162**, 37-49.
- 26 936 Gardés, E., Wunder, B., Marquardt, K. & Heinrich, W. (2012). The effect of water on intergranular mass
27 937 transport: new insights from diffusion-controlled reaction rims in the MgO-SiO₂ system. *Contributions to*
28 938 *Mineralogy and Petrology* **164**, 1-16.
- 29 939 Gasc, J., Brunet, F., Bagdassarov, N. & Morales-Florez, V. (2011). Electrical conductivity of
30 940 polycrystalline Mg(OH)₂ at 2 GPa: effect of grain boundary hydration-dehydration. *Physics and*
31 941 *Chemistry of Minerals* **38**, 543-556.
- 32 942 German, R. M. (2009). Fragmentation behaviour in particulate materials processing. *Powder Metallurgy*
33 943 **52**, 196-204.
- 34 944 Helpa, V., Rybacki, E., Abart, R., Morales, L. F. G., Rhede, D., Jerabek, P. & Dresen, G. (2014).
35 945 Reaction kinetics of dolomite rim growth. *Contributions to Mineralogy and Petrology* **167**.
- 36 946 Hetenyi, G., Cattin, R., Brunet, F., Bollinger, L., Vergne, J., Nabelek, J. & Diament, M. (2007). Density
37 947 distribution of the India plate beneath the Tibetan plateau: Geophysical and petrological constraints on the
38 948 kinetics of lower-crustal eclogitization. *Earth and Planetary Science Letters* **264**, 226-244.
- 39 949 Hiraga, T., Nagase, T. & Akizuki, M. (1999). The structure of grain boundaries in granite-origin
40 950 ultramylonite studied by high-resolution electron microscopy. *Physics and Chemistry of Minerals* **26**,
41 951 617-623.
- 42 952 Joachim, B., Gardés, E., Abart, R. & Heinrich, W. (2011). Experimental growth of **Akermanite** reaction
43 953 rims between wollastonite and monticellite: evidence for volume diffusion control. *Contributions to*
44 954 *Mineralogy and Petrology* **161**, 389-399.
- 45
46
47
48
49
50
51
52
53
54
55
56
57
58
59
60

- 1
2
3 955 Joachim, B., Gardés, E., Velickov, B., Abart, R. & Heinrich, W. (2012). Experimental growth of diopside
4 956 plus merwinite reaction rims: The effect of water on microstructure development. *American Mineralogist*
5 957 **97**, 220-230.
6
7 958 Joesten, R. L. (1991). Kinetics of coarsening and diffusion-controlled mineral growth. *Reviews in*
8 959 *Mineralogy* **26**, 507-582.
9
10 960 John, T. & Schenk, V. (2003). Partial eclogitisation of gabbroic rocks in a late Precambrian subduction
11 961 zone (Zambia): prograde metamorphism triggered by fluid infiltration. *Contributions to Mineralogy and*
12 962 *Petrology* **146**, 174-191.
13
14 963 Lathe, C., Koch-Muller, M., Wirth, R., van Westrenen, W., Mueller, H. J., Schilling, F. & Lauterjung, J.
15 964 (2005). The influence of OH in coesite on the kinetics of the coesite-quartz phase transition. *American*
16 965 *Mineralogist* **90**, 36-43.
17
18 966 Marquardt, K., Ramasse, Q. M., Kisielowski, C. & Wirth, R. (2011). Diffusion in yttrium aluminium
19 967 garnet at the nanometer-scale: Insight into the effective grain boundary width. *American Mineralogist* **96**,
20 968 1521-1529.
21
22 969 Milke, R., Kolzer, K., Koch-Muller, M. & Wunder, B. (2009). Orthopyroxene rim growth between
23 970 olivine and quartz at low temperatures (750-950A degrees C) and low water concentration. *Mineralogy*
24 971 *and Petrology* **97**, 223-232.
25
26 972 Milke, R., Neusser, G., Kolzer, C., Wunder, B. (2013): Very little water is necessary to make a dry solid
27 973 silicate system wet. *Geology* **41**, 247-250.
28
29 974 Molina, J. F., Austrheim, H., Glodny, J. & Rusin, A. (2002). The eclogites of the Marun-Keu complex,
30 975 Polar Urals (Russia): fluid control on reaction kinetics and metasomatism during high P metamorphism.
31 976 *Lithos* **61**, 55-78.
32
33 977 Mueller, H. J., Schilling, F. R., Lauterjung, J. & Lathe, C. (2003). A standard-free pressure calibration
34 978 using simultaneous XRD and elastic property measurements in a multi-anvil device. *European Journal of*
35 979 *Mineralogy* **15**, 865-873.
36
37 980 Ricoult, D. L. & Kohlstedt, D. L. (1983). Structural width of low-angle grain-boundaries in olivine.
38 981 *Physics and Chemistry of Minerals* **9**, 133-138.
39
40 982 Rubie, D. C. (1986). The catalysis of mineral reactions by water and restrictions on the presence of
41 983 aqueous fluid during metamorphism. *Mineralogical Magazine* **50**, 399-415.
42
43 984 Sanchidrian, J. A., Ouchterlony, F., Moser, P., Segarra, P. & Lopez, L. M. (2012). Performance of some
44 985 distributions to describe rock fragmentation data. *International Journal of Rock Mechanics and Mining*
45 986 *Sciences* **53**, 18-31.
46
47 987 Thompson, A. B. (1983). Fluid-absent metamorphism. *Journal of the Geological Society* **140**, 533-547.
48 988 Wood, B. J. & Walther, J. V. (1983). Rates of hydrothermal reactions. *Science* **222**, 413-415.
49 989 Yardley, B. W. D. & Valley, J. W. (1997). The petrologic case for a dry lower crust. *Journal of*
50 990 *Geophysical Research-Solid Earth* **102**, 12173-12185.
51 991 Zinn, P., Lauterjung, J. & Hinze, E. (1995). Kinetic-studies of the crystallization of coesite using
52 992 synchrotron-radiation. *Nuclear Instruments & Methods in Physics Research Section B-Beam Interactions*
53 993 *with Materials and Atoms* **97**, 89-91.
54
55
56
57
58
59
60

Table 1: List of symbols used and their significance

Symbol	Significance	Unit
T	Temperature	K
P	Pressure	Pa
t	Time	s
$\xi(t)$	Reaction progress (comprised between 0 and 1)	no unit
I_i	XRPD peak intensity. Subscripts P and B refer to portlandite and brucite respectively	Counts
χ_i	Weight proportion of phase i . Subscripts P and B refer to portlandite and brucite respectively	no unit
Φ	Calibration factor which relates phase proportion and selected Bragg's reflection intensity ratio	no unit
M_i	Molar weight of phase i , where subscripts P and B refer to portlandite and brucite respectively	g mol^{-1}
J_i	Flux of species i	$\text{mol m}^{-2} \text{s}^{-1}$
D_{CaO}	CaO diffusion coefficient	$\text{m}^2 \text{s}^{-1}$
\bar{D}_{CaO}	Mean effective CaO diffusion coefficient across the reaction front or rim	$\text{m}^2 \text{s}^{-1}$
C_{CaO}	Concentration of CaO species	mol m^{-3}
R	Ideal gas constant	$\text{J mol}^{-1} \text{K}^{-1}$
μ_{CaO}^0	Chemical potential of CaO at the interface between portlandite and the reaction products (i.e., brucite and aragonite)	J mol^{-1}
μ_{CaO}	Chemical potential of CaO at the interface between the reaction products (i.e., brucite and aragonite) and magnesite	J mol^{-1}
$\Delta\mu_{\text{CaO}}$	CaO chemical potential difference across the reaction front or rim	J mol^{-1}
Δx	Reaction front (or rim) thickness	m
ΔG	Free Gibbs energy of the reaction	J mol^{-1}
$\bar{D}_{\text{CaO}}^{\text{GB}}$	Mean grain boundary diffusion coefficient of CaO across the reaction front or rim	$\text{m}^2 \text{s}^{-1}$
l	Grain size of the reaction products, brucite and aragonite, in the reaction front or rim	m
δ	Grain boundary width	m
V_i	Molar volume of phase i with subscripts r , m and p corresponding to the reaction products (i.e., equimolar mix of aragonite and brucite), magnesite and portlandite, respectively	$\text{m}^3 \text{mol}^{-1}$
r_i	Radii used in the spherical geometry. Subscripts A and B refer to the outer and inner radii of the reaction rim respectively and 0 corresponds to the initial magnesite grain radius	m
V_r	Volume of the reaction rim. Can be expressed as the difference between the volumes of the spheres having r_A and r_B for radii	m^3
n_i	Molar amount with subscripts p and m corresponding to portlandite and magnesite, respectively	mol
v	Ratio between molar volumes of magnesite and portlandite, V_m/V_p	no unit
$X(t)$	Reaction progress for a single coarse magnesite grain, comprised between 0 and 1	no unit
Port Ara+Bru	Reaction interface with portlandite on one side and aragonite + brucite on the other	
n	Grain coarsening time exponent, equals to 3 in our case.	no unit
ρ	Grain coarsening constant. Unit depends on n	$\text{m}^3 \text{s}^{-1}$
γ_0	Mean of the natural logarithm of the initial magnesite grain size (with radii log-normally distributed)	no unit
σ	Standard deviation of the natural logarithm of the initial magnesite grain size	no unit

Table 2: Experimental conditions, bulk kinetics and reaction rim growth data, and corresponding diffusivity parameters.

Experiment type	Hydration level	Dataset ^a	Peaks used (Bulk)	T, K	t, s	$t(\xi = 0.5)$, s	$\Delta_r G$, kJ mol ⁻¹	ρ , m ³ s ⁻¹	$D^{GB} \times \delta \pm 1\sigma$, m ³ s ⁻¹ (Bulk)	Δx^b , μm	r_A , μm	r_B , μm	$D^{GB} \times \delta \pm 1\sigma$, m ³ s ⁻¹ (Micro) ^d
		X07	Por Bru	873	1,499	4.50E+01	-41.3	-	2.28E-21 \pm 4.3E-20	-	-	-	-
		X08	Mag Bru Ara	843	6,759	1.90E+02	-41.6	-	4.81E-22 \pm 9.2E-21	-	-	-	-
		X09	Mag Bru Ara	823	9,911	5.10E+03	-42.0	-	9.77E-24 \pm 1.9E-22	-	3.6	1.9 \pm 0.1	9.72E-24 \pm 1.5E-24
	Dry	Y11	Por Bru	833	10,160	4.20E+02	-41.9	-	2.10E-22 \pm 4.0E-21	-	-	-	-
		Y13	Por Bru	833	9,927	1.90E+03	-41.9	-	2.57E-23 \pm 4.9E-22	-	-	-	-
		AA12	Mag Bru Ara	853	279	6.00E+00	-41.6	-	9.49E-21 \pm 1.8E-19	-	5.1	2.3 \pm 0.1	4.44E-22 \pm 5.6E-23
		AA13 ^c	-	823	1,064	-	-42.0	-	-	-	6.8	2.3 \pm 0.1	2.50E-22 \pm 3.1E-23
		X10	Por Bru	823	816	2.00E+00	-42.0	2.72E-22	1.54E-20 \pm 2.2E-19	-	-	-	-
DIA		X11	Por Bru	673	8,739	4.80E+02	-43.2	3.60E-26	7.94E-24 \pm 1.1E-22	-	5.0	2.4 \pm 0.2	6.76E-25 \pm 1.0E-25
		X12	Por Bru	743	408	1.40E+00	-42.8	3.64E-24	2.47E-21 \pm 3.5E-20	-	-	-	-
		X15	Por Bru	573	14,866	2.80E+03	-43.6	6.97E-30	3.31E-26 \pm 4.7E-25	-	-	-	-
		Y09	Por Bru	623	6,267	1.24E+06	-43.5	7.06E-28	1.17E-26 \pm 1.7E-25	-	-	-	-
		Y10	Por Bru	598	8,918	2.16E+06	-43.5	7.72E-29	4.11E-27 \pm 5.8E-26	-	-	-	-
	Intermediate	Y14	Por Bru	673	3,131	9.10E+02	-43.2	3.60E-26	1.28E-24 \pm 1.8E-23	-	-	-	-
		AA9	Mag Bru Ara	648	5,730	1.60E+05	-43.3	5.44E-27	3.98E-26 \pm 5.6E-25	-	10.0	9.0 \pm 0.3	7.04E-26 \pm 6.7E-27
		AA10	Mag Bru Ara	723	4,184	1.40E+04	-42.9	1.07E-24	1.28E-24 \pm 1.8E-23	-	15.0	12.3 \pm 0.1	4.07E-24 \pm 9.0E-26
		AA11	Mag Bru Ara	648	5,218	9.80E+03	-43.3	5.44E-27	2.51E-25 \pm 3.5E-24	-	5.0	4.4 \pm 0.1	2.64E-26 \pm 1.7E-27
		PC182	-	823	234,000	-	-42.0	2.72E-22	-	850 \pm 75	-	-	4.26E-19 \pm 1.2E-19
1D-PC		PC180	-	773	1,897,200	-	-42.5	2.04E-23	-	280 \pm 62	-	-	4.48E-21 \pm 3.9E-21
		PC175	-	873	259,200	-	-41.3	2.70E-21	-	1,380 \pm 125	-	-	2.43E-18 \pm 6.9E-19
PC	Saturated	PC_120	Por Bru	393	-	2.16E+04	-	-	-	-	-	-	-
		PC_150	Por Bru	423	-	6.00E+03	-	-	-	-	-	-	-

^aEach *intermediate* and *dry* conditions DIA dataset corresponds to a single experiment, whereas each of the two *PC saturated* datasets corresponds to a series of quench experiments. 1D-PC data in *intermediate* conditions also correspond to single experiments (see experimental section for details).

^bUncertainties on measurements of reaction front length and rim radii are given as $\pm 1 \sigma$. Error on r_A is the same as for r_B .

^cAA13 was run offline (without synchrotron XRPD) and was therefore not used in the bulk approach. Note that $l = 120$ nm.

^dMost experiments were terminated by increasing the temperature until full reaction completion was observed, which does not allow those samples to be used for the microscopic approach.

For Peer Review

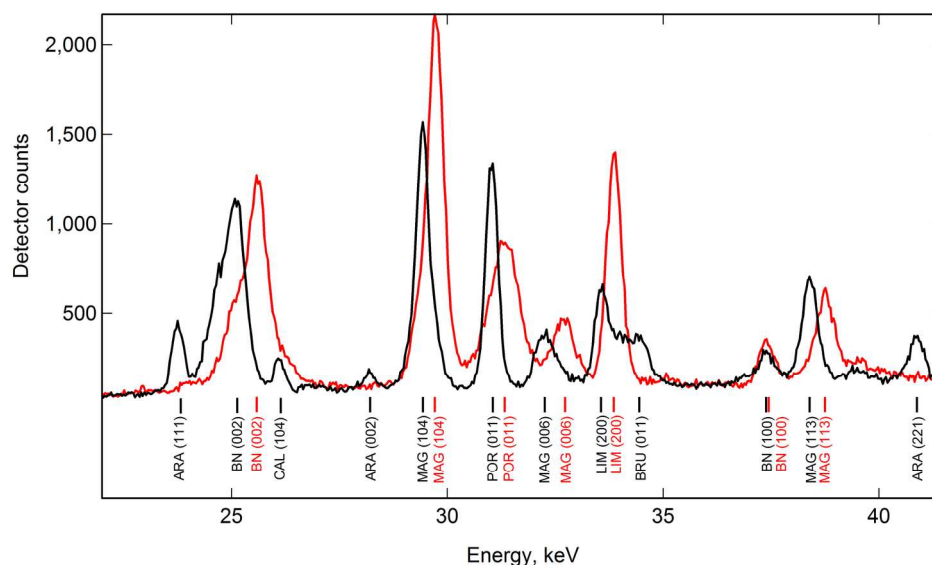


Fig. 1 : XRPD patterns collected on sample Y13 showing the early water activity buffering of the lime (LIM) – portlandite (POR) pair upon heating at 1.8 GPa. MAG, BRU, CAL and ARA stand for magnesite, brucite, calcite and aragonite, respectively. The grey and black patterns correspond to data collected at room temperature and shortly before the target temperature of 833 K was reached, respectively. Note that most peaks are shifted towards lower energies upon heating due to thermal expansion. At ca. 833 K upon heating, small amounts of reaction products, i.e., brucite and aragonite, are present along with minor transient calcite. The persistence of CaO is evidenced by its (200) reflection at 33.85 keV (black pattern), the intensity of which drastically decreased upon heating, as shown by the comparison between the grey and black diffraction patterns, then remained constant during the rest of the experiment. The partial consumption of CaO is interpreted as resulting from the reaction with the sample/assembly water to form Ca(OH)₂. Numbers in parentheses are Miller indices of the diffracting planes.

175x101mm (300 x 300 DPI)

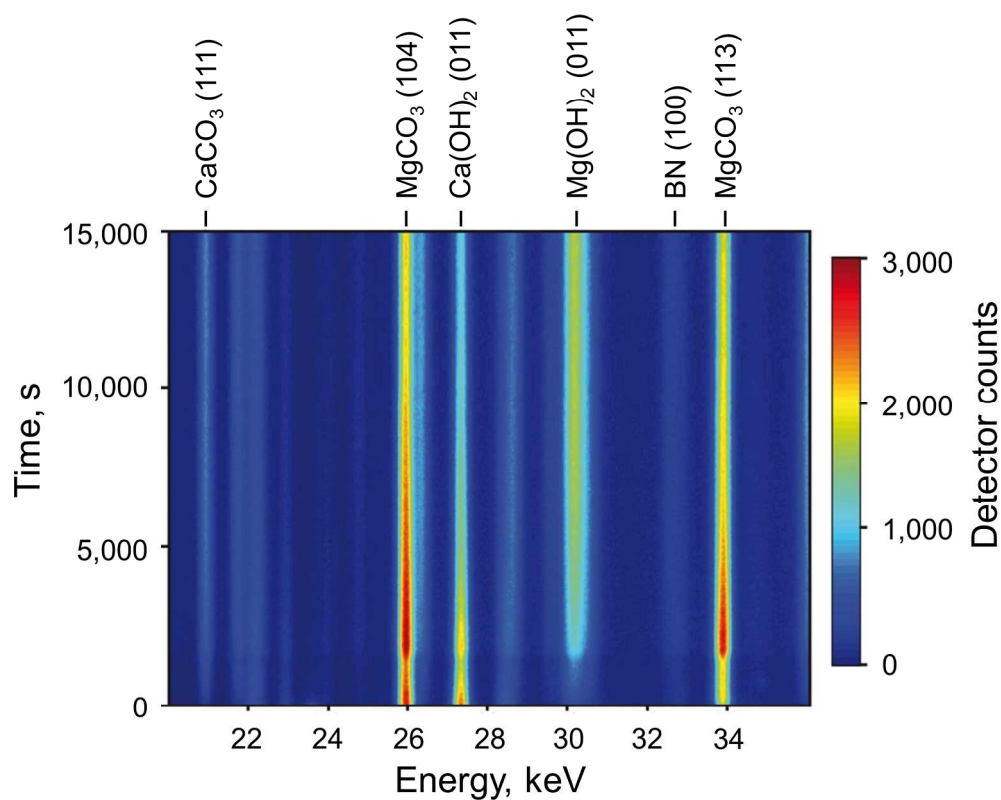


Fig 2 : In-situ XRPD data for Reaction (1) under intermediate conditions at 573 K and 1.8 GPa (run X15).

The spectra were collected with a step time of 45 s. The main diffraction peaks are indexed, including reflections used for the calculation of reaction progress and the BN reflection used for intensity normalization. Note that the corresponding diffraction energies differ from Figure 1 due to a different angle of the detector relative to the incident beam.

198x159mm (300 x 300 DPI)

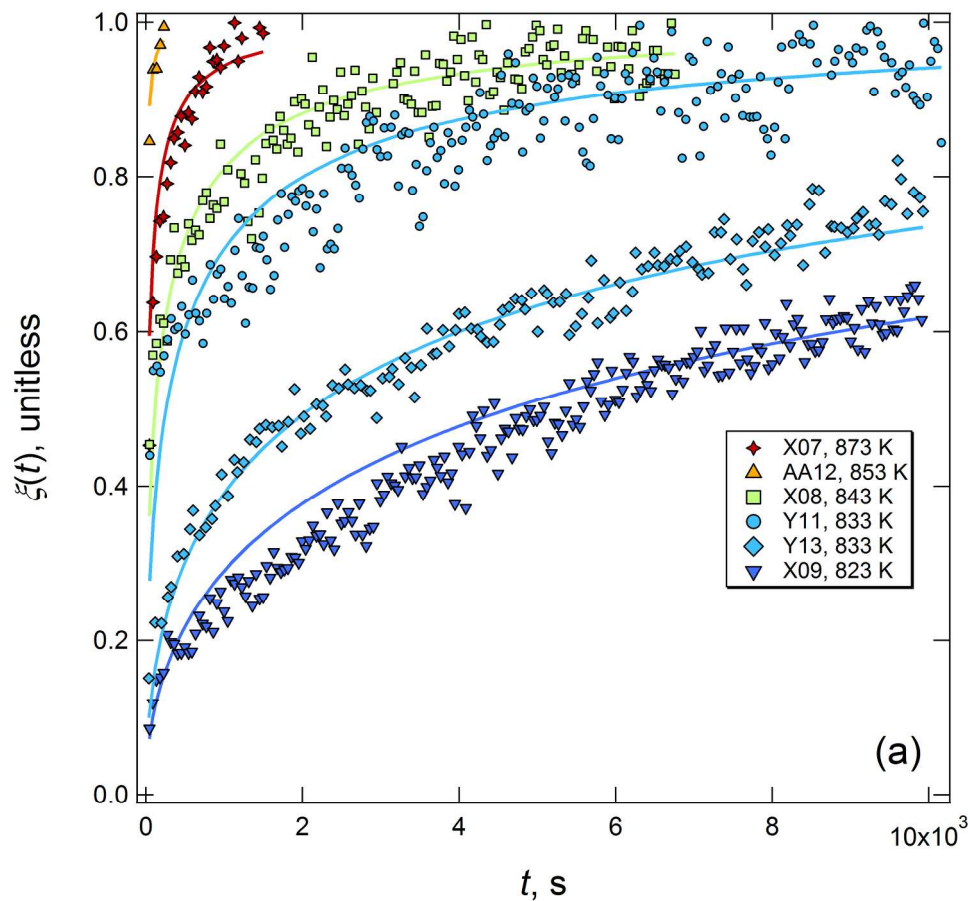


Fig 3a : Bulk kinetic data (reaction progress) and simulated kinetic curves. (a) Dry conditions (DIA); (b) Intermediate conditions (DIA); (c) Saturated conditions (PC). Reaction progress data were obtained from diffraction reflections relative intensities for (a) and (b) (see text for details) and from Equation (4) for (c).

199x181mm (300 x 300 DPI)

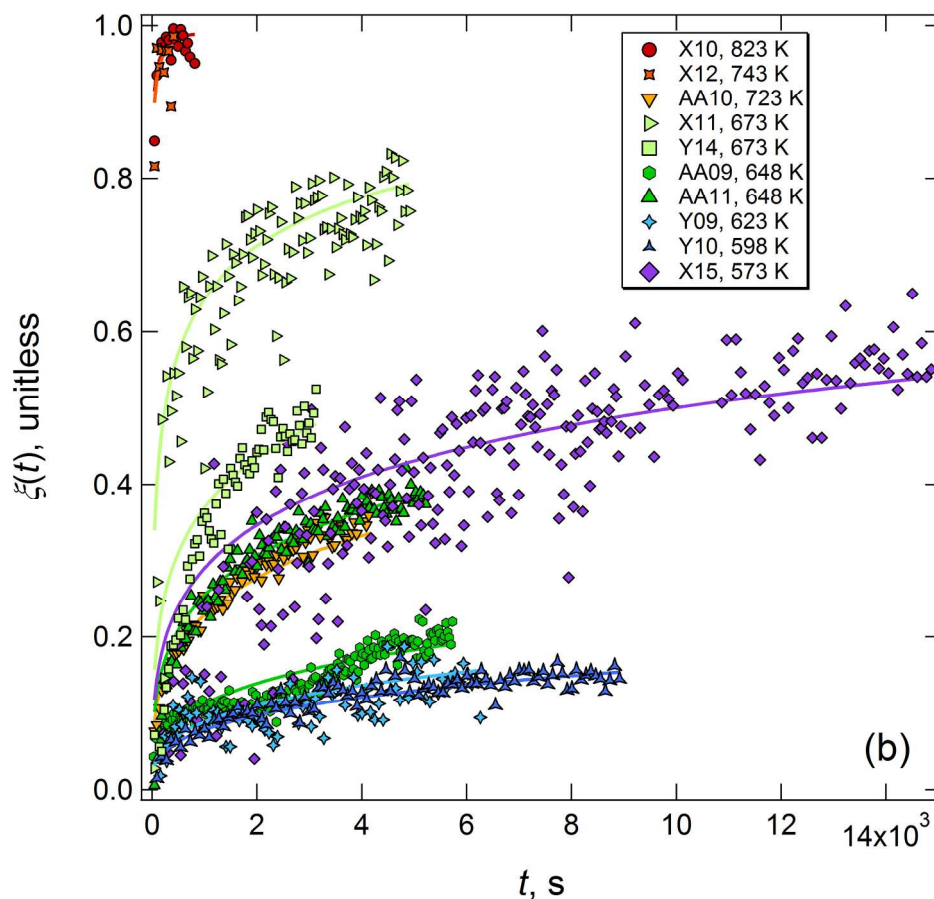


Fig 3b : Bulk kinetic data (reaction progress) and simulated kinetic curves. (a) Dry conditions (DIA); (b) Intermediate conditions (DIA); (c) Saturated conditions (PC). Reaction progress data were obtained from diffraction reflections relative intensities for (a) and (b) (see text for details) and from Equation (4) for (c).

199x181mm (300 x 300 DPI)



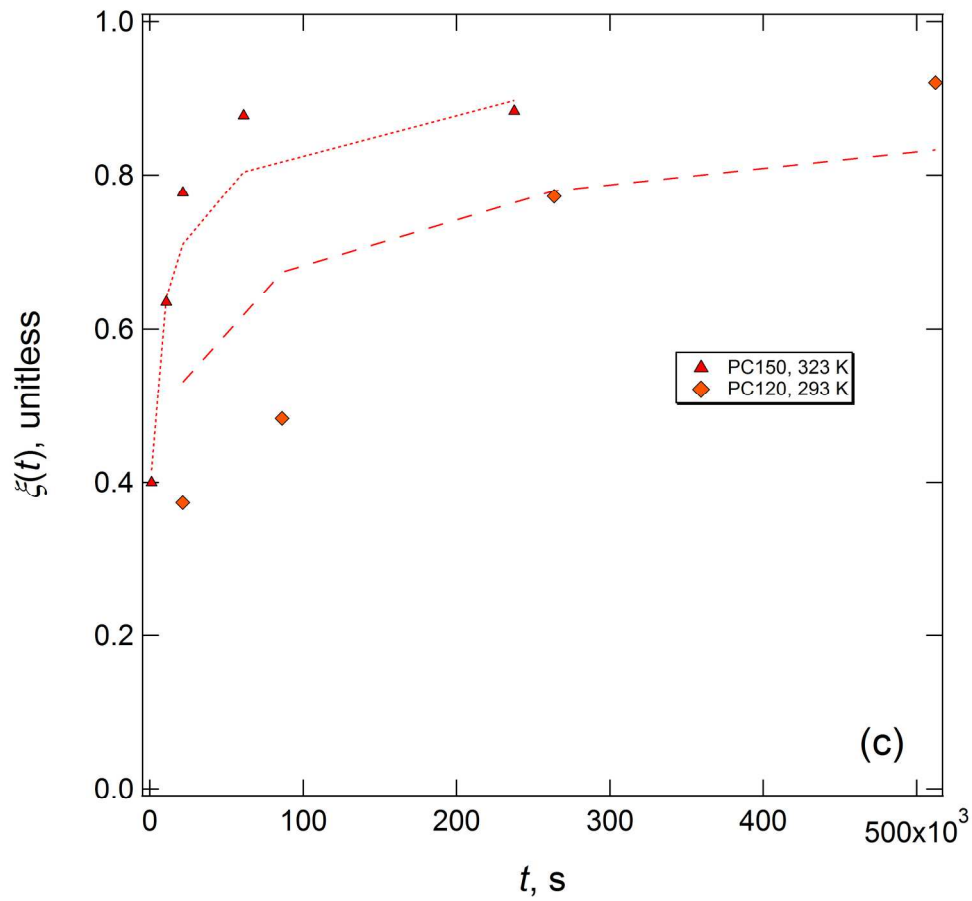


Fig 3c : Bulk kinetic data (reaction progress) and simulated kinetic curves. (a) Dry conditions (DIA); (b) Intermediate conditions (DIA); (c) Saturated conditions (PC). Reaction progress data were obtained from diffraction reflections relative intensities for (a) and (b) (see text for details) and from Equation (4) for (c).

199x181mm (300 x 300 DPI)



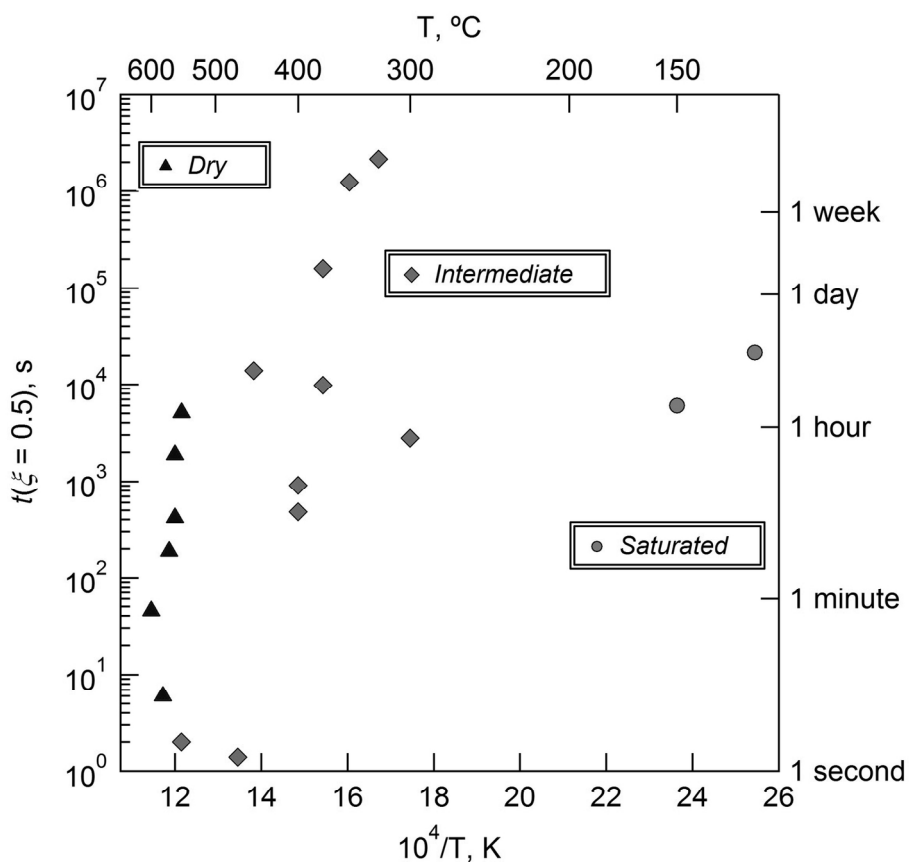


Fig. 4: Half-reaction times obtained from all 16 DIA experiments as well as from the two sets of PC experiments, at 393 K and 423 K.
153x138mm (300 x 300 DPI)

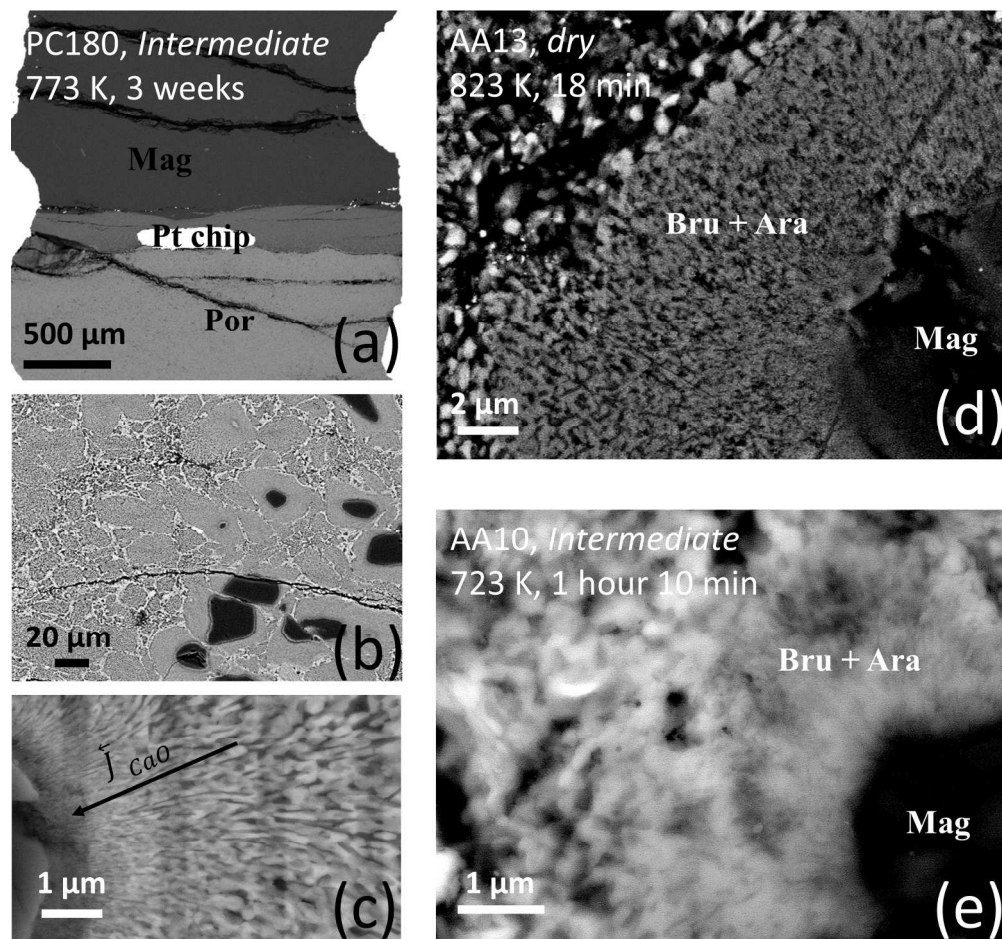


Fig. 5 : FE-SEM images in back-scattered electrons (BSE) mode of recovered samples. Abbreviations Por, Mag, Bru and Ara stand for portlandite, magnesite, brucite and aragonite respectively. (a) 1D-PC sample PC180. The reaction front between Portlandite (lower, bright phase) and $MgCO_3$ (upper dark phase) is visible. The Pt chip (white color) is at the Port | Ara+Bru interface. The fracture network formed upon sample decompression and was not present when the sample reacted. (b) and (c) DIA samples Y10 and Y11, respectively. After collection of the kinetic data (shown in Figure 3) the temperature was increased for both samples to ~ 1073 K (see experimental section for details). (b) As a result these samples show large reaction rims around the coarsest residual magnesite grains. (c) Also thanks to higher temperatures, nicely defined palisade-type rims with brucite and aragonite (darker and brighter phases, respectively) intergrowths are observed. The edge of a residual magnesite grain is visible in the lower left corner. (d) and (e) Detailed views of a reaction rim in samples AA13 and AA10, respectively. The reacting magnesite grain is visible in the bottom lower corner in both cases. Note the finer grain size of the reaction products in (e), due to a lower temperature.

192x179mm (300 x 300 DPI)

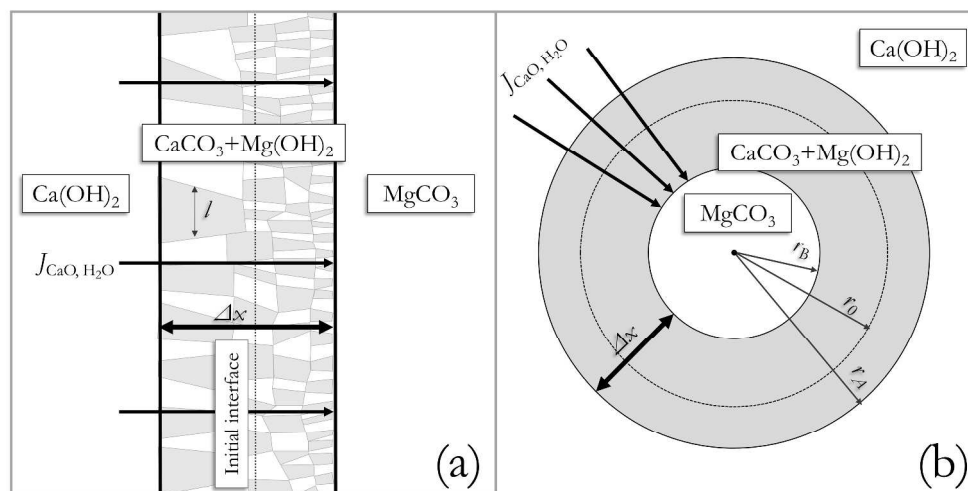


Fig. 6 : Idealized geometries taken for the calculation of D_{CaO}^{δ} . (a) Planar geometry used for calculations of diffusion coefficients from reaction front thickness (1D-PC experiments). (b) Spherical geometry used for the calculation of D_{CaO}^{δ} from reaction rim dimensions (DIA experiments, microscopic approach) and using the analytical solution derived from Abart et al. (2009) to fit the kinetic curves (DIA experiments, macroscopic approach).

338x190mm (300 x 300 DPI)

Review

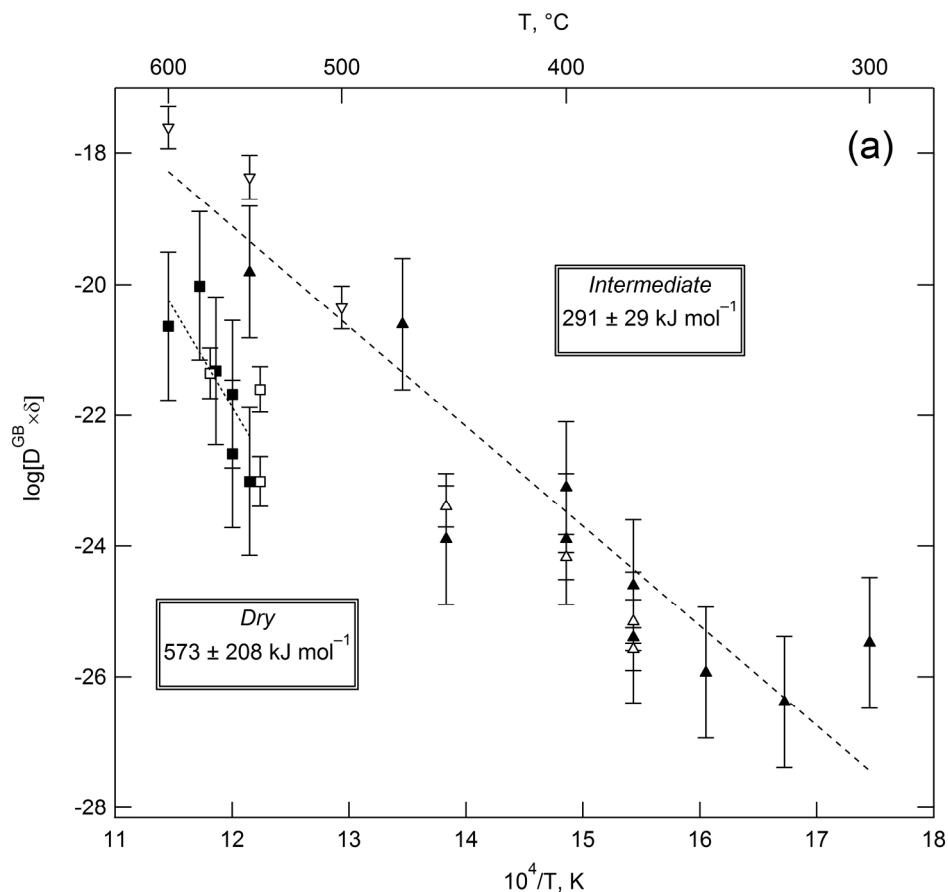


Fig. 7a : Summary of the $D_{CaO}^{GB} \delta$ values obtained in this study and comparison with literature data. (a) Triangles and squares correspond to intermediate and dry data, respectively. Empty symbols represent values retrieved from SEM measurements of reaction rim widths for both intermediate and dry conditions (microscopic approach) with down-pointing triangles representing the 1D-PC data obtained under intermediate conditions. Diffusion data extracted from reaction progress vs. time curves are reported with filled symbols (bulk approach). The dashed lines represent Arrhenius laws obtained by least square fitting of the dry and intermediate data; the activation energies and their respective uncertainties obtained are also labelled. (b) The Arrhenius laws corresponding to our data and shown on (a) are also reported here (same dashed lines) along with grain boundary diffusion data from the literature regarding carbonates: Farver and Yund (1996), Ca diffusion in calcite (empty diamonds); Farver and Yund (1998), O diffusion in calcite (filled diamonds); Helpa et al. (2014), Ca diffusion during dolomite rim growth (empty stars). Additional data were added to illustrate previously demonstrated effect of water content: the black and grey curves and the circle represent diffusion regimes 1, 3 and 4 of Mg in enstatite grain boundaries, as defined in Gardés and Heinrich (2011) and Gardés et al. (2012); these correspond to dry conditions and 0.1-0.5 wt.% and 2.1 wt.% water, respectively.

199x181mm (300 x 300 DPI)

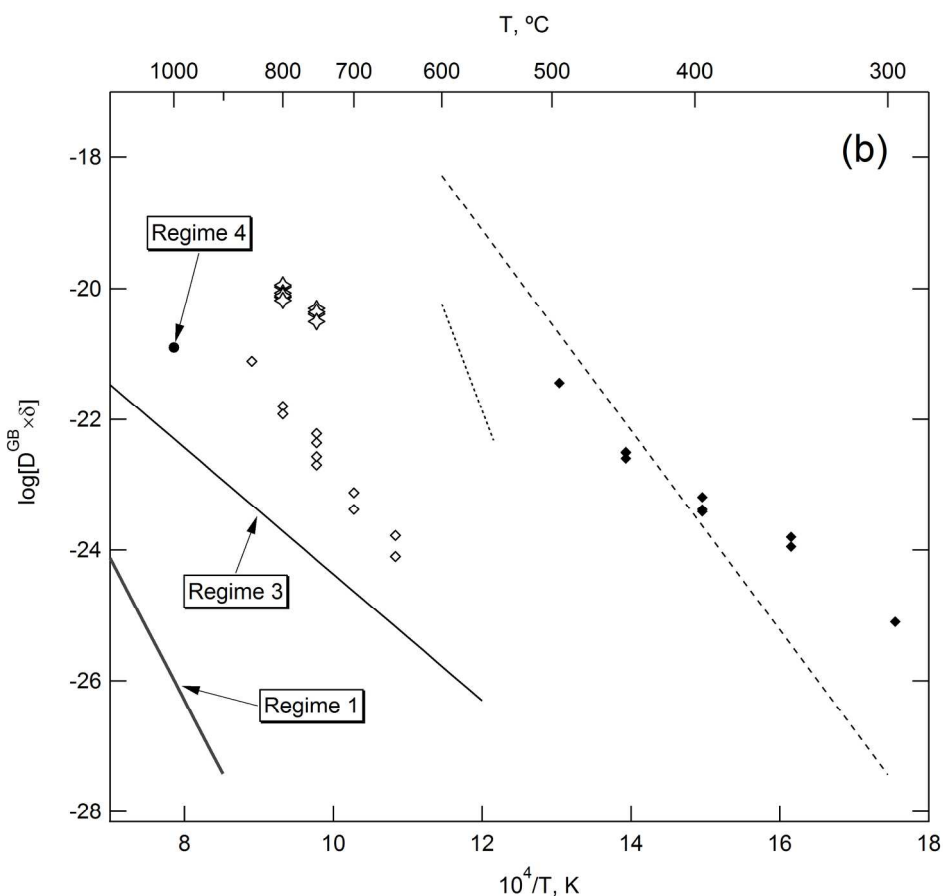


Fig. 7b : Summary of the $D_{CaO}^{GB} \delta$ values obtained in this study and comparison with literature data. (a) Triangles and squares correspond to intermediate and dry data, respectively. Empty symbols represent values retrieved from SEM measurements of reaction rim widths for both intermediate and dry conditions (microscopic approach) with down-pointing triangles representing the 1D-PC data obtained under intermediate conditions. Diffusion data extracted from reaction progress vs. time curves are reported with filled symbols (bulk approach). The dashed lines represent Arrhenius laws obtained by least square fitting of the dry and intermediate data; the activation energies and their respective uncertainties obtained are also labelled. (b) The Arrhenius laws corresponding to our data and shown on (a) are also reported here (same dashed lines) along with grain boundary diffusion data from the literature regarding carbonates: Farver and Yund (1996), Ca diffusion in calcite (empty diamonds); Farver and Yund (1998), O diffusion in calcite (filled diamonds); Helpa et al. (2014), Ca diffusion during dolomite rim growth (empty stars). Additional data were added to illustrate previously demonstrated effect of water content: the black and grey curves and the circle represent diffusion regimes 1, 3 and 4 of Mg in enstatite grain boundaries, as defined in Gardés and Heinrich (2011) and Gardés et al. (2012); these correspond to dry conditions and 0.1-0.5 wt.% and 2.1 wt.% water, respectively.

199x181mm (300 x 300 DPI)

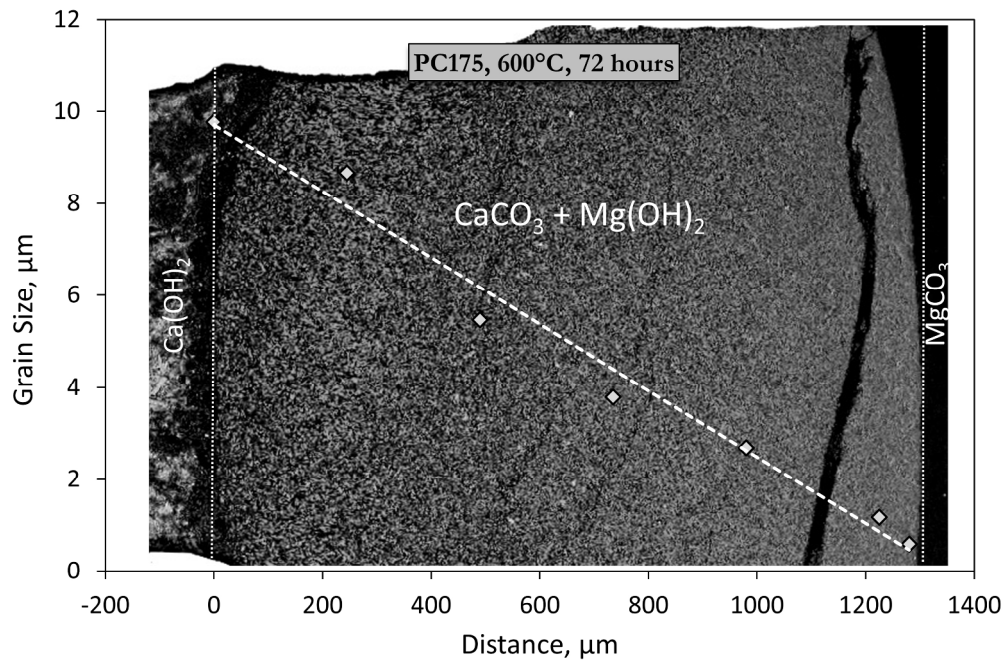


Fig A1 : Grain size of the reaction products across the reaction front in sample PC175. Grain sizes correspond to the average measurement of the five largest identified grains in each location. An SEM backscattered electron image of the reaction front is superimposed to illustrate the grain size gradient.
237x155mm (300 x 300 DPI)

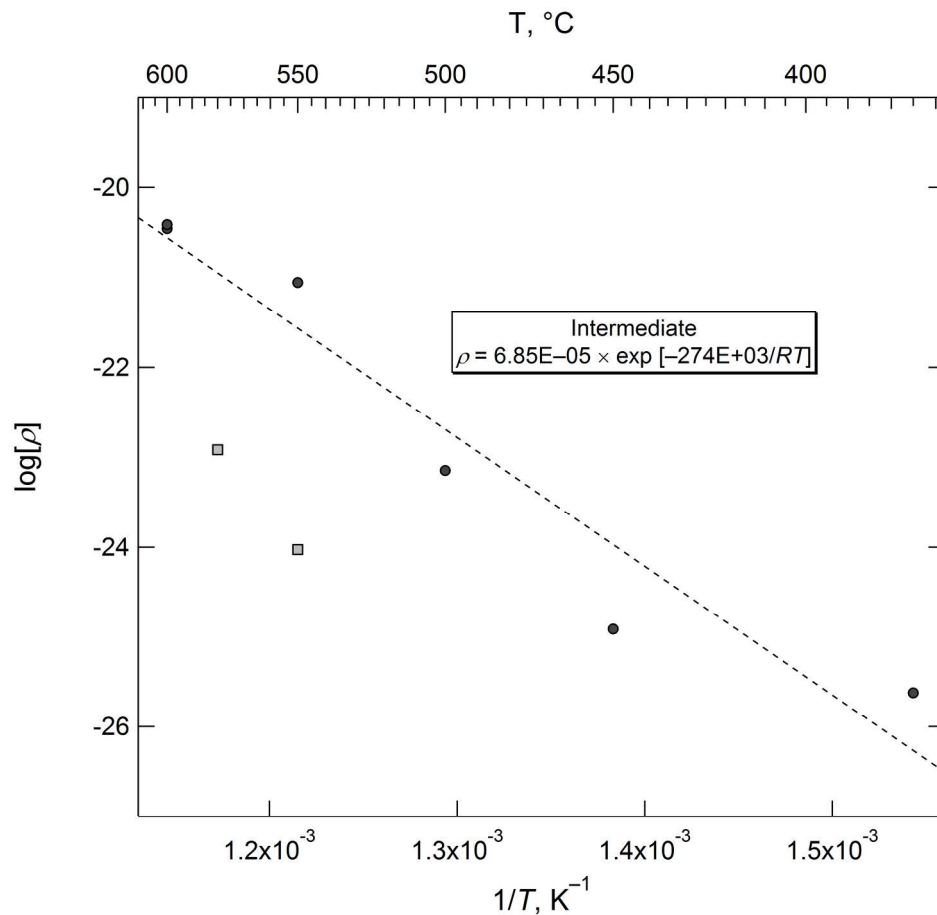


Fig A2 : Arrhenius plot showing the values of ρ obtained from grain size measurements at various temperatures for intermediate and dry experiments (circles and squares, respectively). The linear regression shown by the dashed line returned the values indicated in the adjacent box, according to equation (A3), with Q in $J\ mol^{-1}$.

199x181mm (300 x 300 DPI)

